ACS NANO

www.acsnano.org

ARTICLE

Nicotinamide Adenine Dinucleotide-Loaded Lubricated Hydrogel Microspheres with a Three-Pronged Approach Alleviate Age-Related Osteoarthritis

Yanpeng Lin,▲ Hangtian Wu,▲ Jun Wang,▲ Wanling He, Jiahui Hou, Vidmi Taolam Martin, Chencheng Zhu, Yupeng Chen, Junyuan Zhong, Bin Yu, Aiping Lu, Daogang Guan,* Genggeng Qin,* and Weiguo Chen*

Cite This: *ACS Nano* 2025, 19, 17606−17626

Read Online

ACCESS | Metrics & More | Article Recommendations | Supporting Information

ABSTRACT: Chondrocyte senescence, synovitis, and decreased level of lubrication play pivotal roles in the pathogenesis of age-related osteoarthritis (AROA). However, there are currently no effective therapeutic interventions capable of altering the progression of OA until it reaches advanced stages, necessitating joint replacement. In this study, lubricious and drug-loaded hydrogel microspheres were designed and fabricated by utilizing microfluidic technology for radical polymerization of chondroitin sulfate methacrylate and incorporating nicotinamide adenine dinucleotide (NAD)-loaded liposomes modified with lactoferrin that are positively charged. Mechanical, tribological, and drug release analyses demonstrated enhanced lubrication properties and an extended drug dissemination time for the NAD@NPs@HM microspheres. *In vitro* assays unveiled the ability of NAD@NPs@HM to counteract chondrocyte senescence. RNA sequencing analysis, untargeted metabolomics analysis, and *in vitro* experiments on macrophages revealed that NAD@NPs@HM can regulate the metabolic reprogramming of synovial macrophages, promoting their repolarization from the M1 to M2 phenotype, thereby alleviating synovitis. Intra-articular injection of NAD@NPs@HM in aged mice reduced the mechanisms associated with AROA. These results suggest that NAD@NPs@HM may provide extended drug release, improved joint lubrication leading to better gait, and attenuation of AROA pathogenic processes, indicating its potential as a therapeutic approach for AROA.

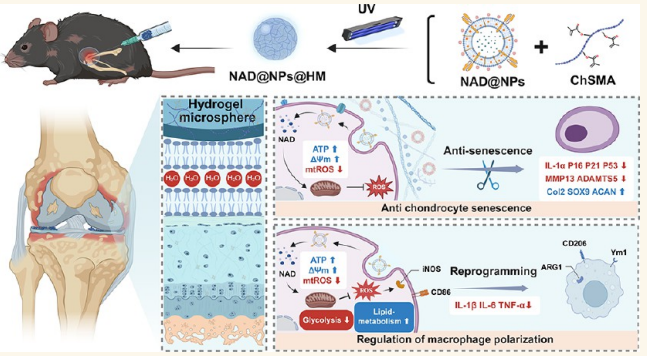

KEYWORDS: *age-related osteoarthritis, nicotinamide adenine dinucleotide, cellular senescence, macrophage reprogramming, lubrication*

INTRODUCTION

It is widely accepted that age is the primary risk factor for the development of osteoarthritis (OA),[1] which is a condition that involves progressive cartilage degeneration and structural−functional deterioration of the entire synovial joint, including its synovium, ligaments, and subchondral bone.[2] Nonetheless, the complex nature of age-related OA (AROA) pathogenesis presents a significant challenge, as there are currently no effective medications available to arrest or decelerate the progression of AROA before it reaches its advanced stage. Consequently, for patients with end-stage knee arthritis, knee replacement surgery frequently emerges as a necessary treatment intervention.[3] However, the inherent risks and substantial financial burdens associated with this surgical procedure cannot be overlooked.[4] Consequently, there exists a pressing, unmet medical need for the development of novel pharmacological interventions aimed at enhancing the efficacy of AROA therapy.

The primary structural and biological constituents of joints encompass cartilage, synovium, and synovial fluid. As organisms age, senescent chondrocytes accumulate prominently in the

Received: January 19, 2025
Revised: April 17, 2025
Accepted: April 17, 2025
Published: May 2, 2025

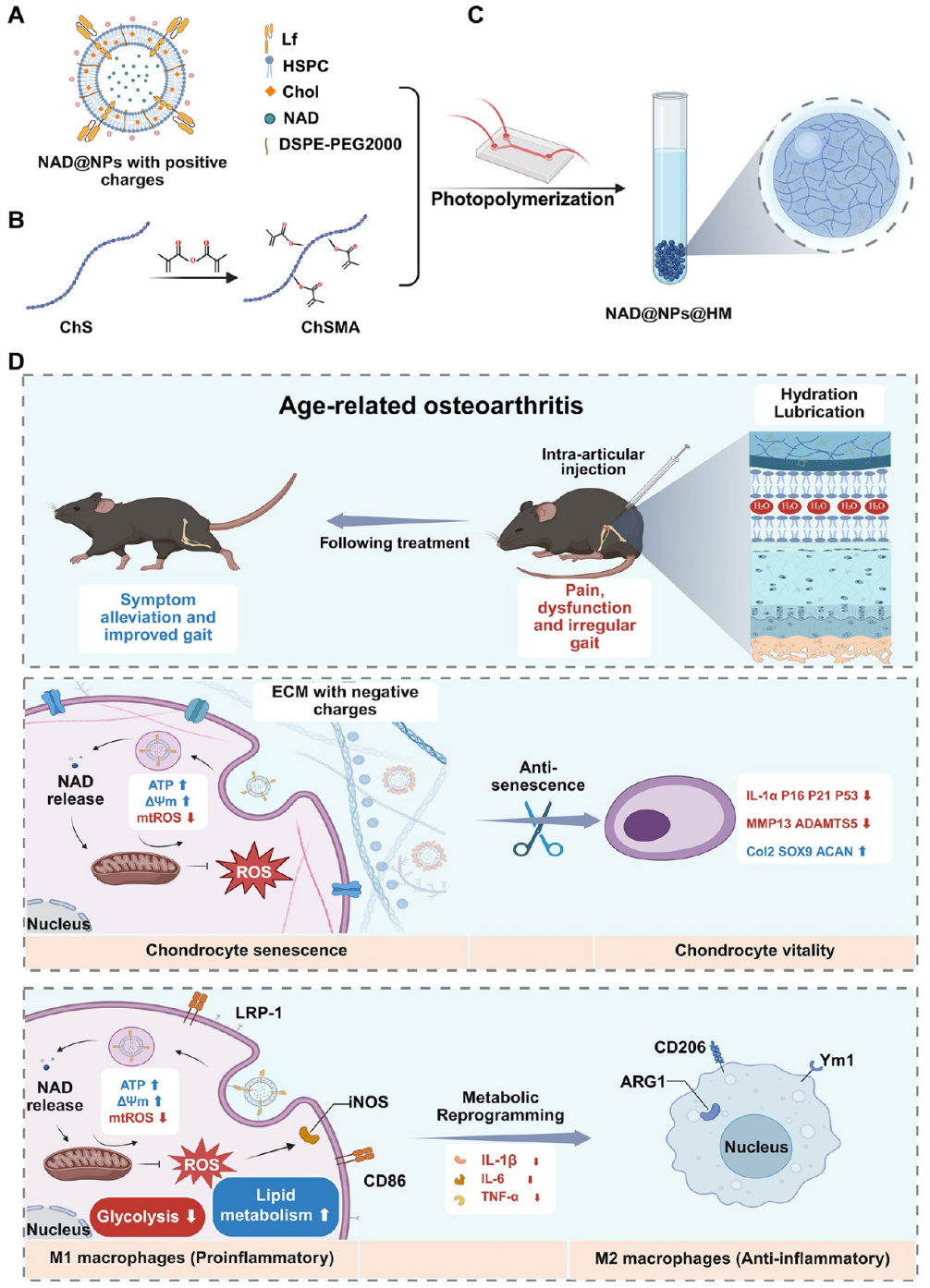

Figure 1. Synthesis protocols and underlying mechanisms of NAD@NPs@HM. (A) The composition of NAD@NPs. (B) Synthesis process of ChSMA. (C) Preparation of NAD@NPs@HM by microfluidic device and photopolymerization process. (D) Mechanistic schema delineating the therapeutic modulation of boundary lubrication, chondrocyte senescence, and macrophage polarization for OA intervention (Created in BioRender. Wu, H. (2025) https://BioRender.com/rr8tovk).

cartilage lesions of elderly individuals and those with OA, causing a decline in cellular proliferation and impairing tissue regeneration and functionality.[5] Senescent chondrocytes exhibit senescence-associated secretory phenotype (SASP), secreting proinflammatory factors and MMPs that drive inflammatory microenvironment formation, oxidative stress, and cartilage degradation.[6] This degradation disrupts the original integrity of the articular cartilage surface, increasing its roughness and susceptibility to erosion.[7,8] This pathological result from extracellular matrix (ECM) degradation fragments activates inflammatory cells, inducing proinflammatory cytokine release and driving synovitis.[9,10] The synovial fluid is secreted by the synovium functions as a biolubricant on the surface of articular cartilage, effectively lubricating the cartilage even under heavy joint loads.[11] However, synovitis alters the composition of synovial fluid, thereby reducing its lubricating efficiency.[12] The increased intra-articular friction resulting from this, in turn, exacerbates synovitis, which further leads to cartilage degeneration.[13] These degradations are accompanied by the development of pain and dysfunction, ultimately resulting in the onset of

https://doi.org/10.1021/acsnano.5c01184
ACS Nano 2025, 19, 17606−17626

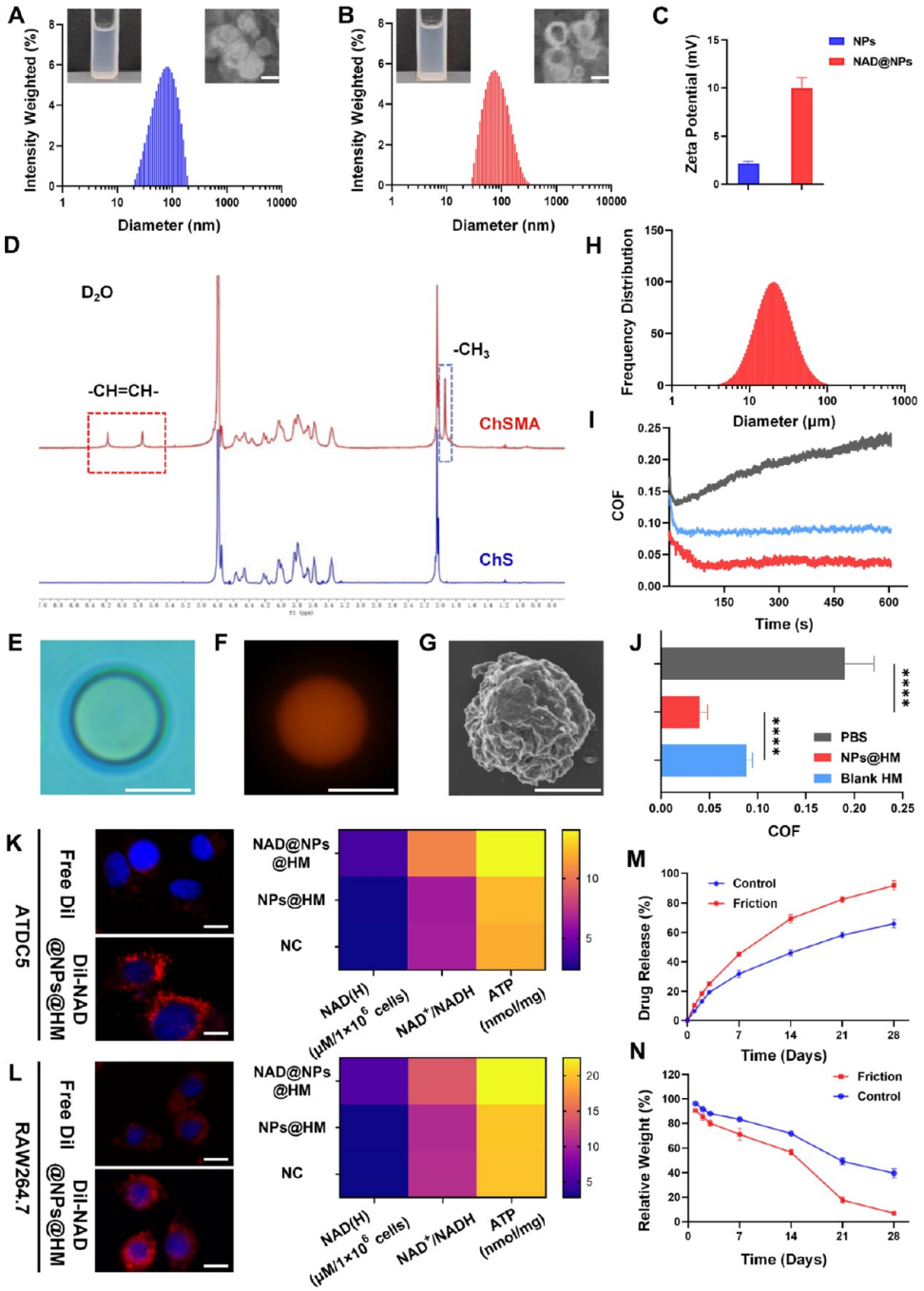

Figure 2. Preparation and characterization of NAD@NPs@HM. (A) A TEM image and the particle size for the blank NPs. (Scale bar: 100 nm). (B) A TEM image and the particle size for the NAD@NPs. (Scale bar: 100 nm). (C) The zeta potential for the blank NPs and the NAD@NPs. (D) ^{1}H NMR spectrum of hydrogel microsphere composition. (E, G) Bright-field plot of NPs@HM, a fluorescent image of Dil-labeled NPs@HM, and a TEM image of NPs@HM. (Scale bar: 25 μm). (H) The particle size for the hydrogel microspheres. (I, J) COF analysis of PBS, blank HM, and NPs@HM. (K, L) Quantification of intracellular NAD(H) level, NAD$^+$/NADH ratio, ATP level, and cellular uptake fluorescent images in chondrocytes and macrophages (scale bar: 50 μm). (M) Drug release profile of NAD@NPs@HM. (N) Degradation curve of NAD@NPs@HM. Data from ≥3 independent experiments (mean ± SD) were analyzed using one-way ANOVA: *P < 0.05, **P < 0.01, ***P < 0.001, ****P < 0.0001.

OA. To interrupt this degenerative loop mechanism, a synergistic therapeutic approach that integrates inhibiting cartilage senescence, regulating synovitis, and enhancing lubrication holds promise as a promising strategy for managing and reversing the progression of AROA.[14]

Nicotinamide adenine dinucleotide (NAD) functions as an essential coenzyme in diverse biochemical redox processes, which are closely associated with energy metabolism.[15] The age-dependent decline in NAD bioavailability contributes to the acceleration of age-related pathologies through dysregulated cellular metabolism.[16] Notably, increasing cellular levels of the metabolic cofactor NAD has been demonstrated to reverse key indicators of aging.[17] Furthermore, NAD also functions as an immune modulator, with increased NAD concentrations capable of alleviating macrophage-mediated inflammation.[18,19] Direct supplementation of the intracellular NAD represents an

https://doi.org/10.1021/acsnano.5c01184
ACS Nano 2025, 19, 17606−17626

attractive strategy for mitigating chondrocyte senescence, inhibiting macrophage-mediated synovitis, and consequently sustaining the homeostasis of the bone microenvironment in the knee joint.[20,21] However, this process has been infrequently explored in the current literature. Moreover, NAD's anionic nature and membrane impermeability mechanistically constrain cellular uptake, necessitating extracellular catabolism into precursors (NAM/NR) for intracellular biosynthesis, thereby requiring supraphysiological concentrations to achieve therapeutic efficacy.[22] Furthermore, intra-articular drug delivery confronts dual physicochemical barriers: anionic dense ECM-mediated penetration resistance and rapid clearance through articular lymphatic-capillary networks.[23] Therefore, in the treatment of AROA, the pressing concerns lie in overcoming these obstacles and augmenting the effective concentration and duration of drugs within the intra-articular cavity.

To address these limitations, we devised a three-pronged AROA treatment strategy that was realized through the utilization of self-lubricating, injectable nanoliposome-encapsulated hydrogel microspheres (Figure 1). Specifically, we selected liposomes as the carrier for NAD and modified them with lactoferrin (Lf), leveraging their substantial benefits, including a lipid bilayer membrane, exceptional biocompatibility, and safety. Lf, an iron-binding glycoprotein ubiquitous in secretory fluids, enters cells via electrostatic interactions between its positive charge and anionic cell surface glycosaminoglycans (GAGs).[24] This mechanism enables Lf-modified nanoparticles (NPs) to target chondrocytes through the ECM charge complementarity. The fabrication of injectable hydrogels has witnessed remarkable advancements in tissue engineering applications, particularly through innovations in biomaterial design that enable superior biocompatibility and precise spatiotemporal regulation of therapeutic payload release.[25] Inspired by this, we engineered photo-cross-linkable chondroitin sulfate-based hydrogel microparticles through methacryloyl-functionalized covalent modification (ChSMA), establishing an injectable intra-articular NPs delivery system. The interfacial interactions between HM polymeric chains and the surrounding aqueous species facilitate the generation of a hydration shell. Subsequently, the incorporation of nanoliposomes into the HM matrix enhances its hydration capacity, thereby resulting in marked tribological properties.[26,27] Furthermore, HM possesses the ability to transform unstable sliding friction into rolling friction, similar to the mechanism of a ball bearing, ultimately minimizing cartilage wear.[28] These microspheres serve as efficient reservoirs for NAD-loaded nanoliposomes, capable of slowly and continuously releasing NAD, thereby significantly extending the effective duration of the drug within the knee joint. This sustained drug delivery provides long-lasting protection against chondrocyte senescence and exhibits anti-inflammatory effects. Concurrently, transcriptome sequencing, metabolomics analysis, and *in vitro* and *vivo* assays revealed that NAD@NPs@HM exhibited targeted suppression of Src-regulated glycolytic flux, initiating a macrophage polarization shift from the M1 pro-inflammatory phenotype toward the M2 anti-inflammatory phenotype. This metabolic modulation consequently attenuated inflammatory cascades while facilitating articular tissue regeneration. We administered this hydrogel microspheres into the knee joints of aged mice and found that NAD@NPs@HM displayed excellent therapeutic effects, as well as good biosafety. In summary, NAD@NPs@HM emerges as a three-pronged for AROA, prolonging intra-articular drug bioavailability, enhancing synovial lubrication for gait optimization, and targeting chondrocyte senescence/macrophage plasticity to mitigate pathological progression.

RESULTS AND DISCUSSION

Preparation and Characterization of NAD@NPs@HM. Phospholipid molecules, including hydrogenated soya phosphatidylcholines (HSPC), can create stable lipid bilayers that decrease friction in synovial fluid, protecting joint cartilage from damage.[29] Compared to traditional lubricants, phospholipid lubrication boasts advantages such as excellent biocompatibility, long-lasting lubrication effects, and friendliness to the joint environment.[30] Hence, we chose HSPC for liposome production because its nanoliposomes create a lubricating film on the cartilage. This film enhances the lubricating property of the articular cartilage and minimizes damage to the cartilage resulting from mechanical friction.[31,32] Conventional liposomes lack targeting functionality and exhibit restricted penetration through articular cartilage's anionic proteoglycan-collagen fibril matrices, prompting the development of lactoferrin-functionalized liposomes.[33] As depicted in Figure 2A,B, both blank NPs and NAD@NPs were spherical when observed under a transmission electron microscopy (TEM) observation, and they had hydrodynamic diameters around 78.52 ± 7.36 and 73.29 ± 2.12 nm, respectively, and the drug loading efficiencies of NAD@NPs were 56.68 ± 3.08% (Table S1). Prior results revealed that nanoliposomes in their unmodified state without Lf bore a negative charge (Table S1). However, upon modification with Lf, the zeta potential of both blank NPs and NAD@NPs shifted, with values of approximately 2.51 ± 0.42 and 9.99 ± 0.87 mV, respectively. These nanocarriers with a positive net charge form weak electrostatic interactions with the anionic ECM surface of cartilage, leading to their adhesion to the cartilage tissue and subsequent retention and penetration throughout the full layer of cartilage.[34,35]

The capacity to sustain an extended retention period and ensure stable drug release within the articular cavity serves as a crucial benchmark for intra-articular injections aimed at OA treatment.[36] To prolong the retention time of nanoliposomes within joints, we embedded them in an injectable hydrogel. We chose chondroitin sulfate, a prevalent glycosaminoglycan in joint cartilage, commonly used for its biocompatibility, anti-inflammatory, and antioxidant effects in joint.[37,38] ChS was functionalized with methacrylic anhydride to yield photo-cross-linkable ChSMA. The successful grafting of methacrylate groups onto ChS was verified by ^{1}H NMR spectroscopy. Methacrylic anhydride (MA) peaks at 5.75 and 6.20 ppm, due to double bond protons, were not present in chondroitin sulfate spectra. Chondroitin sulfate methacrylation was 43%, as shown in Figure 2D. Microfluidic assisted photopolymerization was employed to fabricate the ChSMA microspheres. After being left to stand in solution, the hydrogel microspheres underwent precipitation, and upon gentle agitation, they reconstituted into a uniformly dispersed semitransparent suspension (Figure S1D,E). The hydrogel microspheres were imaged from optical microscopy, which demonstrated that the ChsMA microspheres had the required morphology of intraarticular injection (Figure 2E and Figure S1F) and possessed an average dimension of ≈57.31 ± 3.84 μm (Table S2). To demonstrate the successful incorporation of nanoliposomes into the hydrogel microsphere, a fluorescence microscope was employed to observe the HM containing Dil-stained nanoliposomes. As depicted in Figure 2F, the Dil-stained nanoliposome hydrogel microsphere exhibits an orange-red fluorescence. Upon examination with scanning

https://doi.org/10.1021/acsnano.5c01184
ACS Nano 2025, 19, 17606−17626

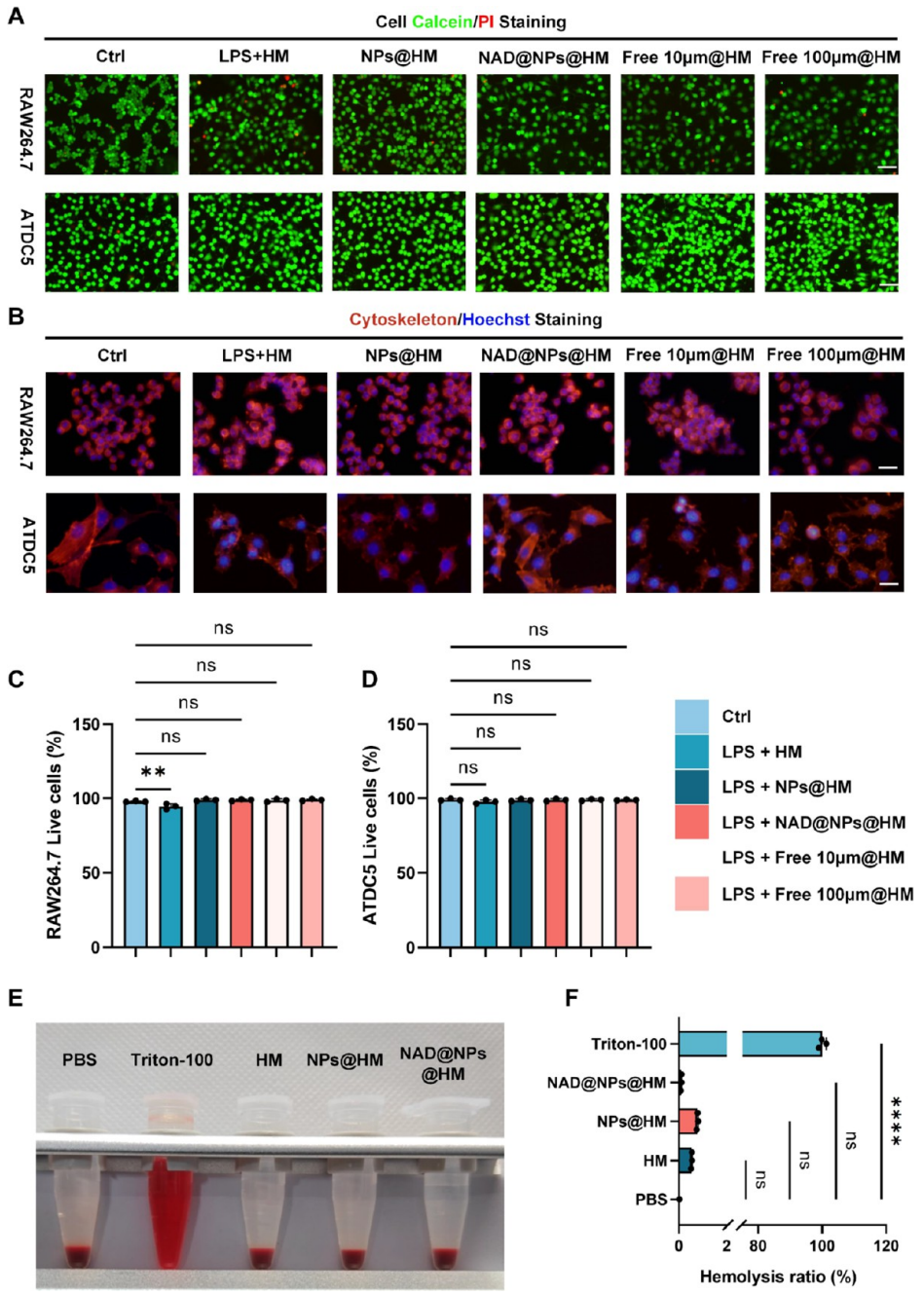

Figure 3. ***In vitro*** **evaluation of NAD@NPs@HM biocompatibility. (A) Viability assessment of ATDC5 chondrocytes and RAW264.7 macrophages in LPS-stimulated models following 24 h culture with hydrogel microsphere formulations (live/dead staining; scale bar: 500 μm). (B) Cytoskeletal organization in microsphere-treated cells (scale bar: 100 μm). (C, D) Quantitative viability analysis. (E) Hemocompatibility evaluation via erythrocyte incubation assay (2 h coculture). (F) Hemolytic ratio quantification. All experiments were performed in triplicate (n = 3). Data represent mean ± SD (*P < 0.05, **P < 0.01, ***P < 0.001, ****P < 0.0001).**

electron microscopy (SEM), the prepared microspheres exhibited a porous spherical morphology (Figure 2G) with nanoliposome aggregates exposed on their surfaces (Figure S1G). These phenomena indicated that the liposomes were successfully loaded into the microspheres. Lubrication deficiency increases friction between joint surfaces, exacerbating cartilage damage and OA progression.[39] Reciprocating tribometry revealed significantly reduced COF values in NPs@HM compared to controls (PBS or HM), with kinetic friction profiles and statistical distributions detailed in Figure 2I,J. The COF for NPs@HM was determined to be 0.040, which was substantially distinct from the COF of blank HM at 0.088 and the PBS group at 0.189. Furthermore, as the friction duration elapsed, the COF of NPs@HM remained stable within a range of 0.03−0.04. This suggests that, as the external hydrogel layer of the microspheres wears away, the encapsulated Lf-modified nanoliposomes continually replenish the lubricating layer, thereby ensuring the material's sustained and stable lubricating properties over time. Overall, the tribological tests showed that NPs@HM improved the lubrication effectively.

NPs tagged with Dil were used to track NAD@NPs@HM in cells, with cell nuclei visualized by using Hoechst 33342. We

https://doi.org/10.1021/acsnano.5c01184
ACS Nano 2025, 19, 17606−17626

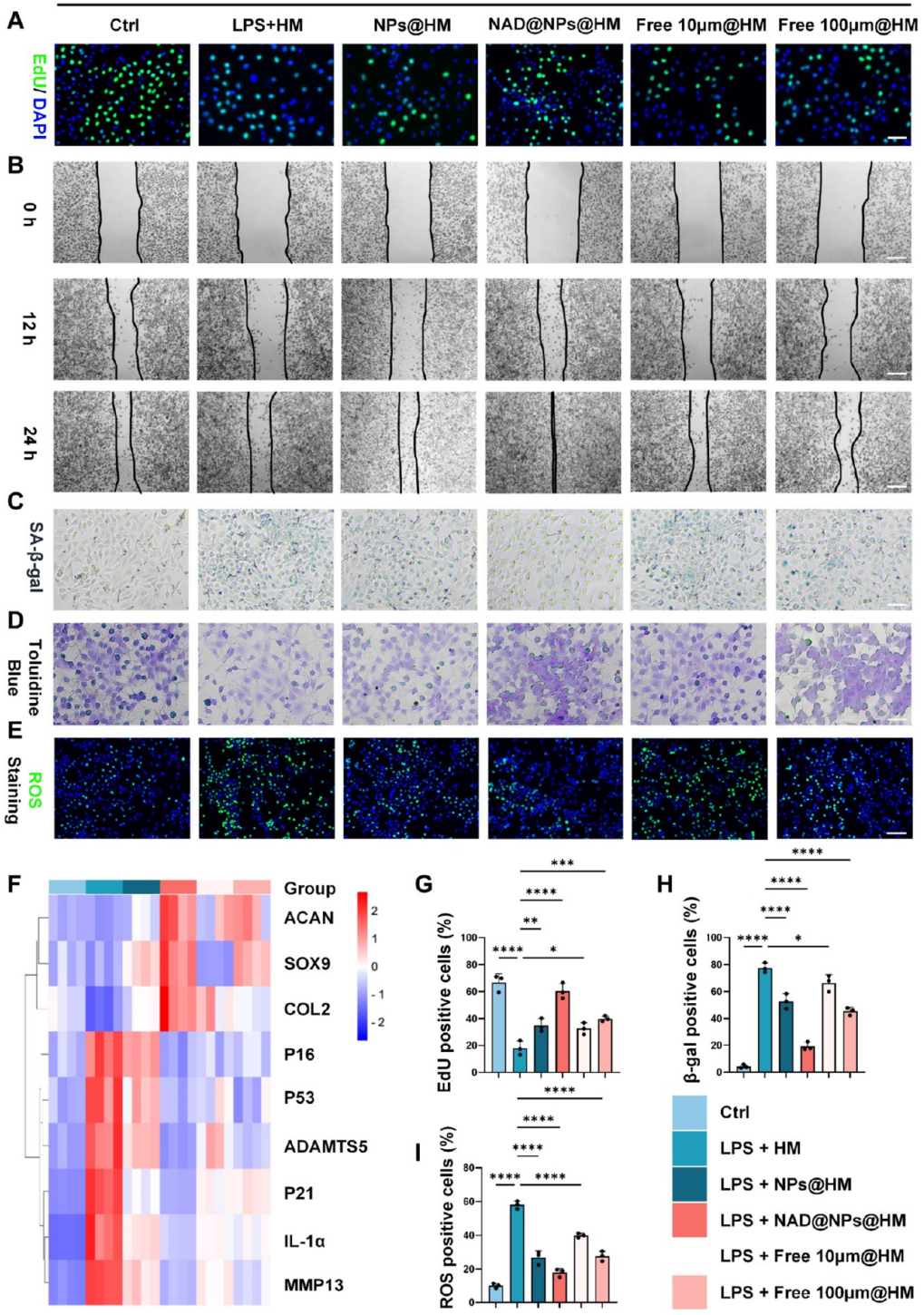

Figure 4. NAD@NPs@HM attenuates chondrocyte senescence and enhances regeneration *in vitro*. (A, B) Edu staining and wound closure of cells cocultured with different hydrogel microspheres. (Scale bar: 500 μm). (C, D) SA-β gal staining and Toluidine blue staining of ATDC5 cell line. (Scale bar: 200 μm). (E) ROS positive cells in ATDC5 chondrocyte cell line. (Scale bar: 500 μm). (F) The expression of chondrocyte anabolic metabolism, catabolic metabolism, and cellular senescence related genes. (G) Statistical quantification of the EdU positive cells. (H) Quantification of the β-gal positive cells. (I) Quantification of the ROS positive cells in ATDC5 chondrocyte cell line. All experiments were performed in triplicate ($n \geq 3$). Data represent mean ± SD (*$P < 0.05$, **$P < 0.01$, ***$P < 0.001$, ****$P < 0.0001$).

evaluated the cellular uptake of NAD@NPs by using RAW264.7 macrophages and ATDC5 chondrocytes. Following 4 h of incubation, both ATDC5 and RAW264.7 cells exhibited intense red fluorescence, suggesting significant cellular uptake (Figure 2K,L). In the incubation with free Dil, only a weak red fluorescence was observed in some cells. This difference is attributed to two factors. First, our approach used Lf as a targeting ligand for delivery, utilizing its natural receptor, LRP-1, which is overexpressed on activated macrophages, enhancing cellular uptake of NAD@NPs through the specific interaction between Lf and LRP-1.[40,41] Second, cationic nanoliposomes form weak electrostatic interactions with the anionic cartilage

https://doi.org/10.1021/acsnano.5c01184
ACS Nano 2025, 19, 17606−17626

ECM, which can overcome the electrostatic barrier and allow entry into the chondrocytes and be rapid ingestion.[42−44] Besides, nanoliposomes' uptake by cells was studied for their impact on NAD(H) levels, NAD^+/NADH ratios, and ATP levels in RAW264.7 and ATDC5 cells, which are key indicators of cellular metabolism and redox status. Notably, NAD-loaded nanoparticles effectively improved cellular NAD(H) levels, raised NAD^+/NADH ratios, and increased ATP levels in both cell types (Figure 2K,L). These nanoparticles showed significant potential in maintaining cellular energy and preventing damage during inflammation.

Drug Release. Ensuring stable drug release and degradation is crucial for managing OA with intra-articular biomaterials.[45] Figure 2M illustrates that both control and friction groups exhibited biphasic drug release, characterized by an initial rapid release followed by prolonged sustained release. Under control conditions, approximately 58% of the nanoliposomes were released from the hydrogel microspheres within 21 days, while this proportion increased to about 82% under frictional conditions, indicating a friction-responsive sustained release. The rapid release in the friction group was attributed to shear force-induced erosion of surface liposomes, while the subsequent sustained release resulted from gradual hydrogel matrix degradation and diffusion of embedded liposomes.[46] This biphasic release behavior aligns with previous studies on shear-responsive hydrogels,[32] where mechanical forces dynamically regulate drug release kinetics through transient pore enlargement and controlled matrix degradation. Similar to prior research,[47] NAD@NPs@HM retained over 28 days even under frictional conditions in a collagenase-containing environment (Figure 2N), indicating reduced biodegradation rates that prolonged its *in vivo* residence time to enable sustained lubrication and therapeutic efficacy. Drug effectiveness is closely related to intra-articular retention duration.[48] IVIS monitoring of Dil-labeled nanoliposome microspheres showed a gradually decreasing fluorescence intensity of NAD@NPs@HM, with weak fluorescence still detectable at 28 days (Figure S2). Both *in vitro* and *in vivo* studies confirmed that the nanoliposome-incorporated hydrogel prolonged retention time, reduced infection risks associated with repeated intra-articular injections, and enhanced sustained lubrication, thereby extending the therapeutic duration of NAD.

Cytotoxicity and Cytocompatibility of NAD@NPs@HM Were Assessed *In Vitro*. To ensure the good biocompatibility of NAD@NPs@HM as an implantable lubricating biomaterial, it was imperative to assess its cytotoxicity and cytocompatibility in chondrocytes *in vitro*. Viability assessment via live/dead staining (Figure 3A) and subsequent quantification (Figure 3D,E) demonstrated >95% cellular survival in both RAW264.7 macrophages and ATDC5 chondrocytes across all hydrogel formulations after 24 h culture, with nonsignificant variation between experimental groups. This underscores the excellent cytocompatibility of the hydrogel microspheres. Furthermore, cytoskeleton staining results revealed no discernible variations in cell morphology for both cell lines when incubated with various hydrogel microspheres compared to the control group (Figure 3B). Notably, all hydrogel microspheres exhibited hemocompatibility with hemolysis ratios below 2%, substantially lower than the 5% safety threshold specified by ASTM F756-08 standards (Figure 3F,G). This underscores the excellent cytocompatibility of the hydrogel microspheres.

NAD@NPs@HM Attenuates Chondrocyte Senescence and Enhancing Regeneration *In Vitro*. Articular cartilage undergoes senescence and decay over time, with the number of senescent chondrocytes exhibiting a strong correlation with age.[49] Cellular senescence is commonly characterized as an irreversible cessation of the cell cycle in response to replicative stress and the process of aging.[50] We coincubated various hydrogel microspheres with chondrocytes in senescent conditions. EdU staining revealed a notable decrease in the percentage of EdU-positive cells when induced by LPS (Figure 4A,G), indicating a decrease in the cellular proliferative capacity. The number of newly proliferating EdU-positive cells in the NAD@NPs@HM group (with an equivalent concentration of NAD at 10 μm) was higher than those in Ctrl, HM, NPs@HM, free 10 μm@HM, and free 100 μm@HM. This was further confirmed by the CCK8 assay (Figure 4H). The results of a scratch assay indicated that NAD@NPs@HM exhibited higher migration rates (Figure 4B and Figure S3F). Therefore, NAD@NPs@HM may play an essential role in promoting chondrocytes regeneration. Subsequently, Toluidine blue staining and senescence β-galactosidase staining (SA-β-Gal) were assessed in chondrocytes treated with distinct hydrogel formulations under senescence-inducing conditions. As depicted by the SA-β-Gal staining in Figure 4C,H, the NAD@NPs@HM group exhibited a limited number of blue-stained spots approaching baseline levels observed in normal controls. In stark contrast, significantly higher quantities of stained masses were detected in the other groups. Similarly, Toluidine blue staining (Figure 4D) revealed an increased intensity of staining in the cartilage matrix of the NAD@NPs@HM, demonstrating enhanced proteoglycan deposition within the chondrocyte extracellular matrix. Notably, the NAD@NPs@HM group demonstrated substantial upregulation of COL2A1 and a notable decrease in MMP13 and ADAMTS5 levels in chondrocytes induced by LPS, closely mirroring the trends observed in the NC group (Figure 4F). Furthermore, aggrecan, a crucial structural component of the extra chondral matrix, and SOX9, which governs cartilage development, exhibited significant elevations in mRNA expression in chondrocytes treated with NAD@NPs@HM. Consequently, NAD@NPs@HM can significantly enhance chondrocyte proliferation and migration, exert chondroprotective effects, and inhibit chondrocyte senescence.

Mitochondrial dysfunction, characterized by a reduced transmembrane potential, is associated with cellular aging and serves as a key indicator of it. This leads to increased ROS production, worsening mitochondrial damage and dysfunction and creating a vicious cycle.[51,52] Therefore, we examined the condition of aging chondrocytes by measuring the mitochondrial membrane potential and their sensitivity to oxidation. The protective potential of NAD@NPs@HM was evidenced by the potent red fluorescence and weak green fluorescence due to JC-1 accumulation in the mitochondria (Figure S3A). ROS staining with DCFH-DA demonstrated the remarkable ROS scavenging capacity of the NAD@NPs@HM group compared to that of the positive control (Figure 4E,I). Elevated generation of mtROS renders mitochondrial DNA more prone to mutations. This not only interferes with the process of ATP synthesis but also leads to mitochondrial malfunction, eventually culminating in ATP shortage.[53] Similarly, mitochondrial ROS (mtROS) staining with MitoSOX red also revealed the superior mtROS scavenging ability of the NAD@NPs@HM group (Figure S3A). We found that NAD@NPs@HM effectively sustained the NAD level (Figure S3B) and enhanced the cellular ATP level (Figure S3D) in senescent chondrocytes and improved the ATP supply as well as cell viability for cells (Figure S3E) undergoing oxidative stress

https://doi.org/10.1021/acsnano.5c01184
ACS Nano 2025, 19, 17606−17626

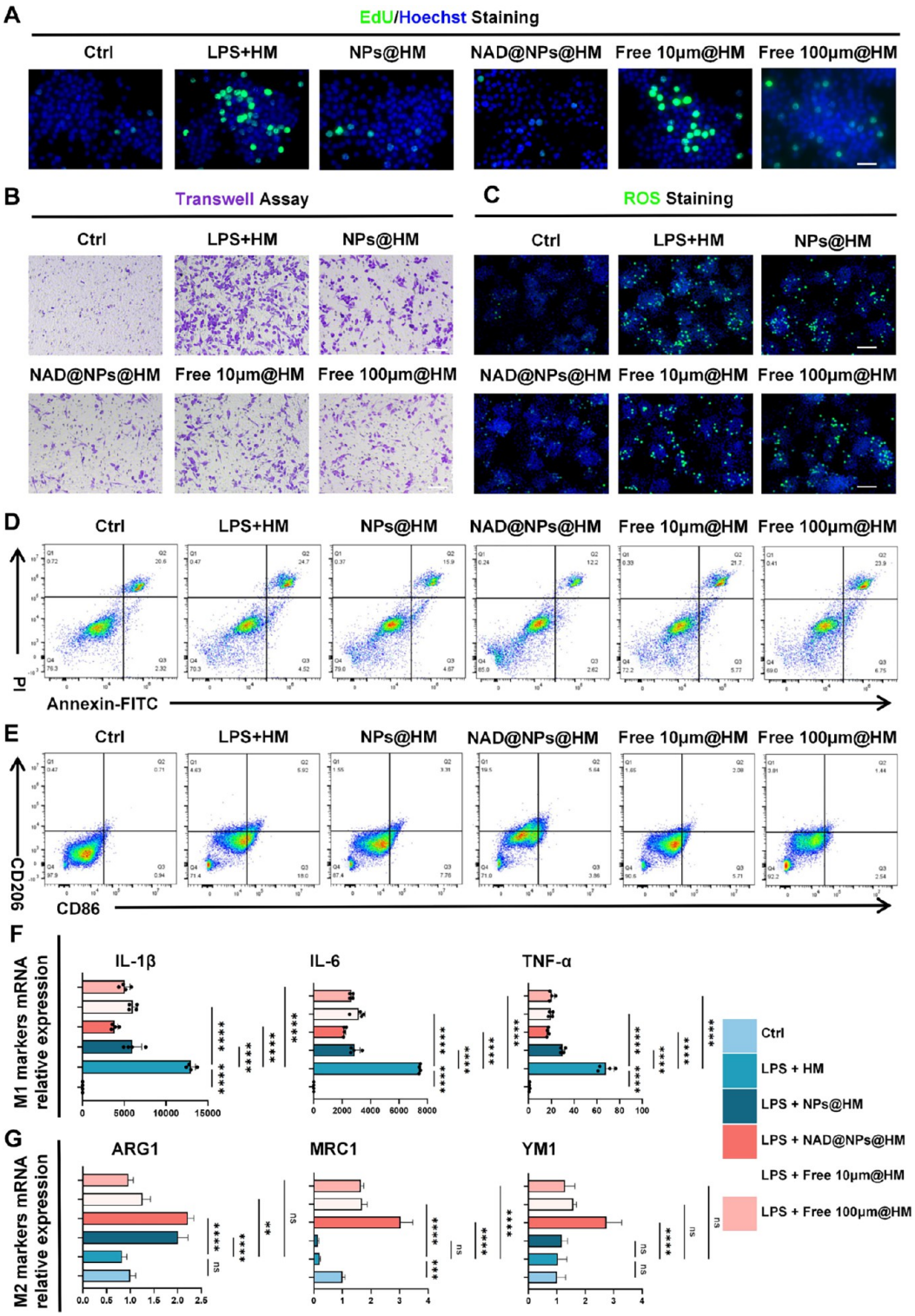

Figure 5. NAD@NPs@HM regulates inflammation in LPS-stimulated macrophages. (A) EdU staining in RAW264.7 cell line after coculture with different hydrogel microspheres in LPS-mediated cellular inflammation model (scale bar: 200 μm). (B) Transwell assay in RAW264.7 cell line. (Scale bar: 500 μm). (C) ROS positive cells in RAW264.7 cell line. (Scale bar: 500 μm). (D) Flow cytometry detection of cell apoptosis. (E) Flow cytometry detection of macrophage types. (F, G) The expression of M1 or M2 macrophage marker genes. All experiments were performed in triplicate ($n \geq 3$). Data represent mean ± SD (*$P < 0.05$, **$P < 0.01$, ***$P < 0.001$, ****$P < 0.0001$).

or NAD depletion. Furthermore, heightened ROS levels stimulate the sustained release of vast quantities of SASP cytokines, which are detrimental to cellular health.[54,55] The expression levels of pivotal SASP genes, including IL-1α, P16, P21 and P53, were significantly increased in LPS-induced senescent chondrocytes (Figure 4F). These SASP-related factors, in conjunction with excess ROS, are extruded into the extracellular milieu, fostering a localized pathological microenvironment. This not only accelerates the senescence of adjacent normal chondrocytes but also intensifies mitochondrial

https://doi.org/10.1021/acsnano.5c01184
ACS Nano 2025, 19, 17606−17626

damage, thereby culminating in a vicious cycle of cellular senescence,[56] ultimately contributing to the gradual degeneration of the ECM.[57] In addition, as illustrated by the qPCR findings, NAD@NPs@HM could significantly reduce the expression of these factors, thereby alleviating the phenotypes associated with chondrocyte senescence.

Consequently, NAD@NPs@HM effectively reverses the senescence process of chondrocytes by promoting chondrocyte proliferation, migration, and matrix secretion while downregulating SASP gene expression and mitigating mitochondrial damage, thereby enhancing the ATP levels and cellular viability of chondrocytes.

NAD@NPs@HM Blocks the Inflammatory Cascade and Regulates of Macrophages M1-to-M2 Polarization *In Vitro*. Synovitis is linked to cartilage degeneration and is key in OA pathogenesis.[58] The main feature is the buildup of numerous activated M1 macrophages in the synovial membrane, which secrete proinflammatory factors and MMPs and engage with chondrocytes.[59,60] While NAD has been implicated in inflammation, the precise role it plays, whether suppressing or exacerbating inflammation, remains a subject of ongoing debate.[22,61,62] To address this query, we exposed LPS-stimulated RAW264.7 cells to different hydrogel microspheres. Our goal was to assess whether NAD@NPs@HM could mitigate the features of proinflammatory cytokines under in vitro conditions. Consistently, the levels of NAD(H) (Figure S4C) and ATP (Figure S4E) were reduced in the LPS-activated macrophages. The number of activated macrophages correlated with OA severity pain and stiffness.[63] In our study, we utilized a CCK-8 assay (Figure S4B) along with Edu staining (Figure 5A and Figure S4F) to assess the proliferation of RAW 264.7 cells when treated with various hydrogel microsphere groups. The results showed that after LPS activation, NAD@NPs@HM effectively inhibited the proliferation of RAW 264.7 cells. This finding was further confirmed by transwell assay results (Figure 5B). These results demonstrate that NAD@NPs@HM can attenuate the proliferation and migration of activated macrophages.

The activation of the macrophage by LPS triggers mitochondrial dysfunction, resulting in heightened ROS production and oxidative stress, thereby markedly enhancing macrophage polarization toward the M1 phenotype.[64,65] To assess the integrity of mitochondrial function, we measured the depolarization of the mitochondrial membrane potential using JC-1 as a probe. Figure S4A indicates that cells exposed to LPS have intense green fluorescence and diminished red fluorescence, suggesting that LPS causes mitochondrial membrane depolarization. However, cells receiving NAD@NPs@HM treatment show markedly enhanced red fluorescence, suggesting our approach effectively alleviates mitochondrial dysfunction caused by LPS and maintains normal mitochondrial activity. Oxidative stress and chronic inflammation constitute the ultimate common pathway underlying the development of OA.[55] We further assessed the antioxidative effects of our nanoliposome hydrogel microspheres on RAW264.7 cells by evaluating their efficacy in scavenging ROS by using DCFH-DA as a probe. LPS was incubated with RAW264.7 cells to induce oxidative stress. The green fluorescence signaling in different treated cells was detected by a fluorescence microscope and depicted in Figure 5C and Figure S4G, and a noticeable increase in the ROS signal was observed in the LPS-treated group, indicating that LPS successfully induced cellular oxidative stress. In contrast, treatment with NAD@NPs@HM led to a significant reduction in fluorescence, providing strong evidence for their ability to effectively mitigate intracellular ROS production and exhibit potent antioxidative properties. Similarly, treatment with NAD@NPs@HM significantly reduced the mtROS level of LPS-activated macrophages (Figure S4A).

To further investigated the impact of our NAD@NPsHM on the anti-inflammatory effect of RAW264.7 cells, we analyzed the apoptosis of the macrophage cells in each treatment group by flow cytometry. Our findings revealed that the anti-inflammatory effect of the nanoliposome hydrogel microspheres did not stem from an increase in macrophage apoptosis (Figure 5D). Macrophages are crucial for balancing inflammation by changing their polarization states, which can be broadly classified into two distinct subtypes: M1 and M2. In the chronic inflammatory microenvironment of OA, macrophages often have difficulty undergoing smooth polarization from the M1 to M2 state, resulting in a significantly elevated ratio of M1 to M2 macrophages in synovial fluid in knee OA patients compared to the healthy control.[66] These findings indicate that an imbalance between M1 and M2 synovial macrophages is strongly correlated to the severity of OA, leading us to investigate whether our nanoliposome hydrogel microspheres possess the capability to regulate macrophage polarization. LPS-activated macrophages *in vitro*, polarized toward the M1 phenotype, secrete an array of proinflammatory cytokines, notably IL-1β, IL-6, and TNF-α. These cytokines, in turn, promote inflammation, chondrocyte senescence, and ECM degradation, leading to the deterioration of cartilage and the advancement of OA.[67,68] The LPS-treated group exhibited a significant upregulation of these proinflammatory cytokines, suggesting an M1 state in macrophages. However, NAD@NPs@HM significantly reduced the level of secretion of IL-1β, IL-6, and TNF-α (Figure 5F), demonstrating a potent anti-inflammatory effect attributed to cytosolic NAD delivery, while the expression of M2 macrophages surface markers such as MRC1 (CD206), YM1, and ARG1 was significantly increased after NAD@NPs@HM treatment. It is worth noting that even the empty NPs@HM showed a reduction in cytokine production, which aligns with previous studies reporting that lipid-coated NPs can sequester LPS, thereby partially mitigating its inflammatory effects.[69,70] Additionally, we observed a concentration-dependent downregulation of inflammatory factor expression in the free NAD treatment group (Figure 5F). To further monitor macrophage polarization, the expression levels of M2 marker CD206 and M1 marker CD86 were evaluated using flow cytometry. As depicted in Figure 5E and Figure S4H,I, NAD@NPs@HM elevated the proportion of $CD206^{+}CD86^{-}$ M2 macrophages while decreasing the proportion of $CD206^{-}CD86^{+}$ M1 macrophages, resulting in a significant increase in the M2/M1 ratio. This finding validates the repolarizing effect of our NAD@NPs on macrophages.

In summary, macrophages treated with NAD@NPs@HM following LPS exposure exhibited elevated total NAD levels and an altered NAD^{+}/NADH ratio. This led to enhanced ATP production, maintenance of mitochondrial function and homeostasis, and reduction in ROS production. Furthermore, the treatment modulated macrophage polarization, downregulating M1 proinflammatory genes while upregulating M2 macrophage-specific genes.

NAD@NPs@HM Regulated the Transcriptomics of Macrophages. To understand how NAD@NPs@HM affects macrophage polarization, we evaluated the differentially expressed genes in the control group, the LPS plus HM (model) group, and the LPS plus NAD@NPs@HM (treatment) group

https://doi.org/10.1021/acsnano.5c01184
ACS Nano 2025, 19, 17606−17626

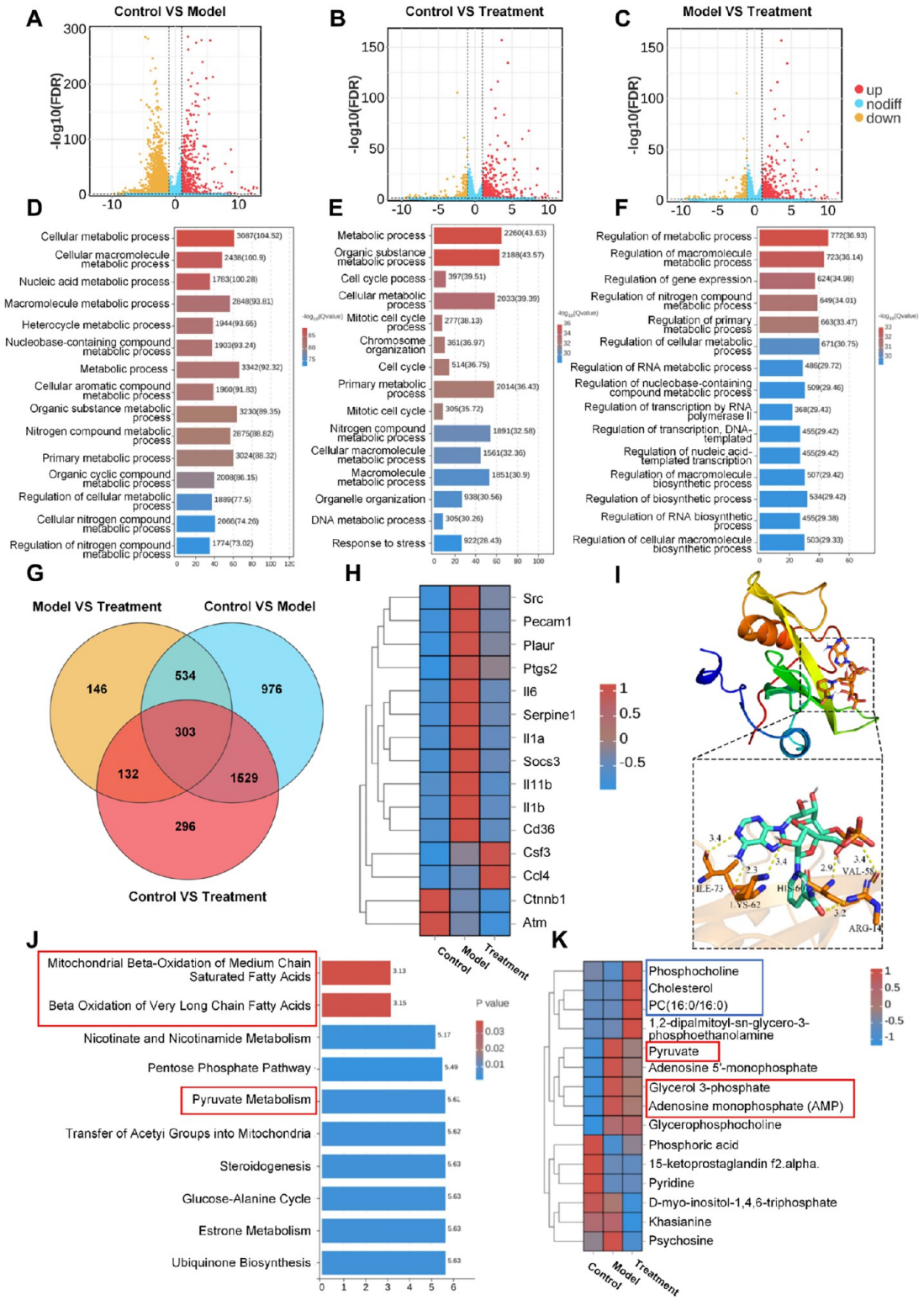

Figure 6. NAD@NPs@HM regulates the transcriptomics and metabolomics of macrophages stimulated with LPS. (A−C) Volcano plot of differentially expressed genes. (D−F) GO enrichment analysis of transcriptional alterations. (G) Venn diagram related to genes involved in cellular metabolic processes. (H) The expression of the top 15 hub genes in the network. (I) Molecular interactions between NAD and c-Src, including binding interface and allosteric modulation sites. (J) Metabolite set enrichment analysis among the groups. (K) Analysis of the top 15 differential metabolites among the groups.

using mRNA-seq. The resultant principal component analysis (PCA) plot showed tight clustering among the five replicates within each group, with clear segregation observed among the three distinct groups, control, model, and treatment, indicating substantial differences at the transcriptome level (Figure S5A). Differential gene expression analysis showed that, compared to the control group, the treatment group had 3645 differentially expressed genes (764 upregulated, 2881 downregulated), the

https://doi.org/10.1021/acsnano.5c01184
ACS Nano 2025, 19, 17606−17626

model group had 5251 (525 up, 4726 down), and when comparing the model and treatment groups, there were 1734 genes (1550 up, 184 down) with differential expression (Figure 6A−C, Figure S5B). The gene ontology analysis identified several terms related to cellular metabolism in pairwise comparisons of differentially expressed genes, as illustrated in Figure 6D−F. The corresponding NAD binding was upregulated in the GSEA enrichment meta-analysis when comparing the model and treatment group (Figure S5C). Moreover, 303 differentially expressed genes, which are associated with cellular metabolism, were identified as common among the comparison groups (Figure 6G). Using MCODE, the most significant modules were extracted from a protein−protein interaction (PPI) network. Subsequently, 10 core gene targets were identified using CytoHubba, namely, SRC, PECAM1, PLAUR, PTGS2, IL6, SERPINE1, IL1A, IL1B, CSF3, and CCL4 (Figure S5E). As depicted in the heatmap illustrating differential gene expression (Figure 6H), the expression of IL-1α, IL-1β, IL-6, and IL-11 that belonged to the interleukins family decreased significantly by NAD@NPs@HM. We observed that Src, a hub gene, was highly expressed in the model group, but its expression returned to near control levels in the treatment group. The physiological Src proto-oncogene, also known as c-Src, is a protein-tyrosine kinase that plays key roles in cellular metabolism, cell growth, division, migration, and survival signaling pathways.[71] Similar to previous findings (Figures 5A,B and 6H), following treatment with NAD@NPs@HM, the expression of Src genes in LPS-activated macrophages was significantly downregulated, leading to decreased cellular proliferation and migratory capabilities and consequently exhibiting an anti-inflammatory effect. Chen et al.[72] found that SRC may link lipid metabolism and macrophage polarization. Inhibiting Src effectively can significantly reduce LPS-induced macrophage activation and also affect M2 macrophage polarization.[73,74] Molecular docking simulations predicted NAD and Src binding affinities, yielding binding free energy values ranging from −6.411 to −5.801 kcal/mol (Table S4). The findings indicate that Src plays a pivotal role in inflammatory responses mediated by macrophages, and the anti-inflammatory properties of NAD@NPs@HM may control macrophage polarization through the modulation of Src.

NAD@NPs@HM Regulates the Metabolomics of Macrophages Stimulated with LPS. To further study the metabolic changes in LPS-induced macrophages affected by NAD@NPs@HM, we used an untargeted metabolomics approach. OPLS-DA analysis was utilized to distinguish between the control group, the model group, and the treatment group. The resulting OPLS-DA score plot demonstrated tight clustering of the five replicates within each respective group as well as distinct separation among the three differing groups (Figure S6A−C). This separation indicates a distinct metabolic signature of the control, model, and treatment groups. The composite scatter plot (Figure S6D), which visualizes the overall alterations in metabolites conducting pairwise analyses, uses orange and green colors to indicate downregulated and upregulated metabolites, respectively. Metabolomic heatmap analysis revealed significant intergroup variations in metabolite abundance, with downregulated (red) and upregulated (blue) compounds clustered by differential expression patterns (Figure 6K). Previous research has demonstrated that M1 and M2 macrophages display unique metabolic profiles that are distinctly different from those of macrophages in their resting state.[75,76] Upon stimulation with LPS, resting macrophages undergo a phenotypic shift toward a proinflammatory M1 state, which is reliant on glycolysis. Conversely, the activation of M2 macrophages is contingent upon fatty acid oxidation.[77] Similarly, our findings revealed a significant elevation in both adenosine monophosphate (AMP) and pyruvate (PA)—the ultimate product of glycolysis—in M1 macrophages within the model group. In the treatment group, within the blue box highlighting significantly distinct metabolites, an increase in the lipid metabolite content was observed, accompanied by a notable decrease in AMP and pyruvate levels (Figure 6K). The results of metabolite enrichment analysis indicated that the treatment group tended to focus on β-oxidation of medium-chain fatty acids and ultra long chain fatty acids in mitochondria (Figure 6J). These results suggested that NAD@NPs@HM can reprogram LPS-induced M1 macrophages into M2 macrophages *in vitro* through metabolic reprogramming. This process entails an augmentation in lipid metabolism, thereby transforming M1 macrophages, which originally exhibited a tendency toward aerobic glycolysis, into M2 macrophages.[77] The PA content detection kit (Solarbio, China) was used to further verify the PA content (Figure S6E). Given the role of Src in cellular metabolic reprogramming, qPCR was employed to assess the expression levels of Src and the key glycolytic enzyme hexokinase 2 (HK2) in each group. Similarly, Src and HK2 were highly expressed in the model group and lowly expressed in the treatment group (Figure S6F,G). Src can interact with HK2 and phosphorylate it. This phosphorylation modification generally increases the catalytic activity of HK2, thereby enhancing its affinity for glucose and promoting glucose uptake and the glycolytic process.[78] Using O2PLS for joint analysis of transcriptome and metabolome data (Figure S6H), the resulting gene-metabolite association loading plot revealed tight clustering of hub genes and differential metabolites, indicating a close correlation between hub genes and differential metabolites. These data revealed that NAD@NPs@HM modulates the Src-HK2 pathway, inhibiting glycolysis catabolism and promoting fatty acid β-oxidation in LPS-stimulated macrophages, thereby inducing metabolic reprogramming in M1 macrophages and driving a phenotypic shift toward the M2 type.

NAD@NPs@HM-Treated Macrophages Against Chondrocyte Degeneration. To explore the potential protective effects of NAD@NPs@HM-treated macrophages against cartilage degeneration, we developed a coculture system comprising macrophages and ATDC5 cells (Figure S7A). Initially, ATDC5 cells were exposed to LPS conditions, followed by the addition of macrophages that had been stimulated with LPS alone (designated as the CM-LPS group) or LPS in combination with NAD@NPs@HM (CM-NAD@NPs@HM group), along with their respective conditioned media, to the chondrocytes. The β-gal staining (Figure S7B) demonstrated a notable increase in the number of senescent chondrocytes in the CM-LPS group, whereas macrophages treated with LPS plus NAD@NPs@HM inhibited the degeneration of ATDC5 cells in the presence of LPS. Toluidine blue staining (Figure S7C) revealed enhanced proteoglycan deposition within chondrocytes of the LPS plus NAD@NPs@HM group, while the results of a scratch assay indicated higher migration rates for this group (Figure S7D,E). The expression levels of key SASP genes (IL-1α and P21), the cartilage synthesis gene (COL2A1), and the cartilage degradation gene (MMP13) were further evaluated. As shown in the qPCR results (Figure S7F), the CM-NAD@NPs@HM group exhibited decreased expression of SASP genes and the cartilage degradation gene compared with the other groups,

https://doi.org/10.1021/acsnano.5c01184
ACS Nano 2025, 19, 17606−17626

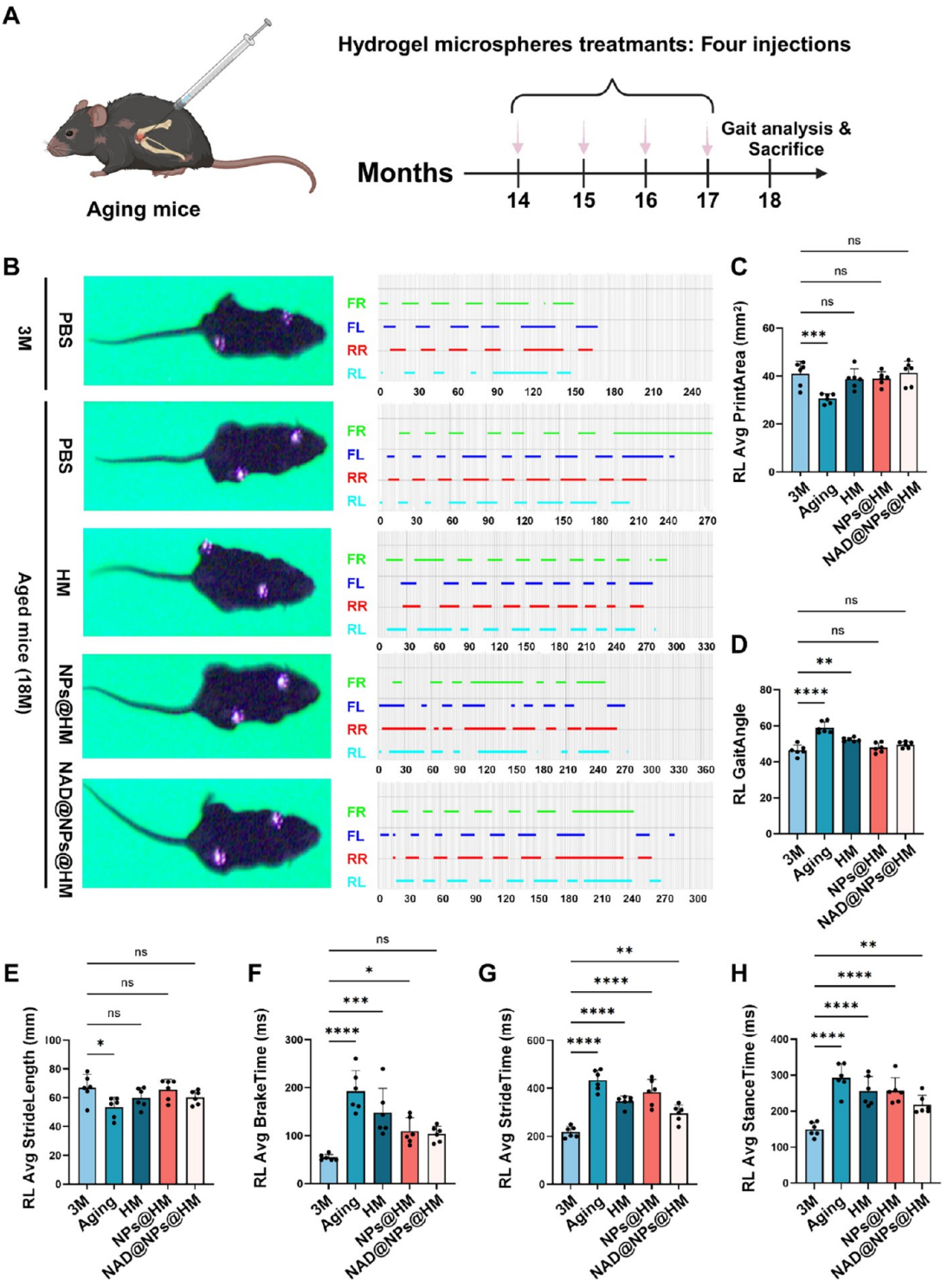

Figure 7. Gait analysis for the mice after intra-articular injection with hydrogel microspheres. (A) Methodological workflow for establishing the AROA murine model (Created in BioRender. Wu, H. (2025) https://BioRender.com/rr8tovk). (B) Representative gait screen shot and gait intensity. (C) Quantification of Rear Left limb average print area. (D) Quantification of Rear Left limb gait angle. (E) Quantification of Rear Left limb average stride length. (F) Quantification of Rear Left limb average brake time. (G) Quantification of Rear Left limb average stride time. (H) Quantification of Rear Left limb average stance time. Data are represented as means ± SD ($n = 6$). FR: front right limb. FL: front left limb. RR: rear right limb. RL: rear left limb.

accompanied by an increase in the expression of the cartilage synthesis gene. These data indicate that macrophages activated by LPS and treated with NAD@NPs@HM can significantly mitigate chondrocyte senescence, demonstrating its great potential in the treatment of AROA.

Biosafety Assessments *In Vivo*. The biocompatibility of NAD@NPs@HM was evaluated through the histology of major organs, blood routine tests, and blood biochemistry analyses in mice. After various treatments, histopathological evaluation of major organs (heart, liver, spleen, lungs, and kidneys) revealed

https://doi.org/10.1021/acsnano.5c01184
ACS Nano 2025, 19, 17606−17626

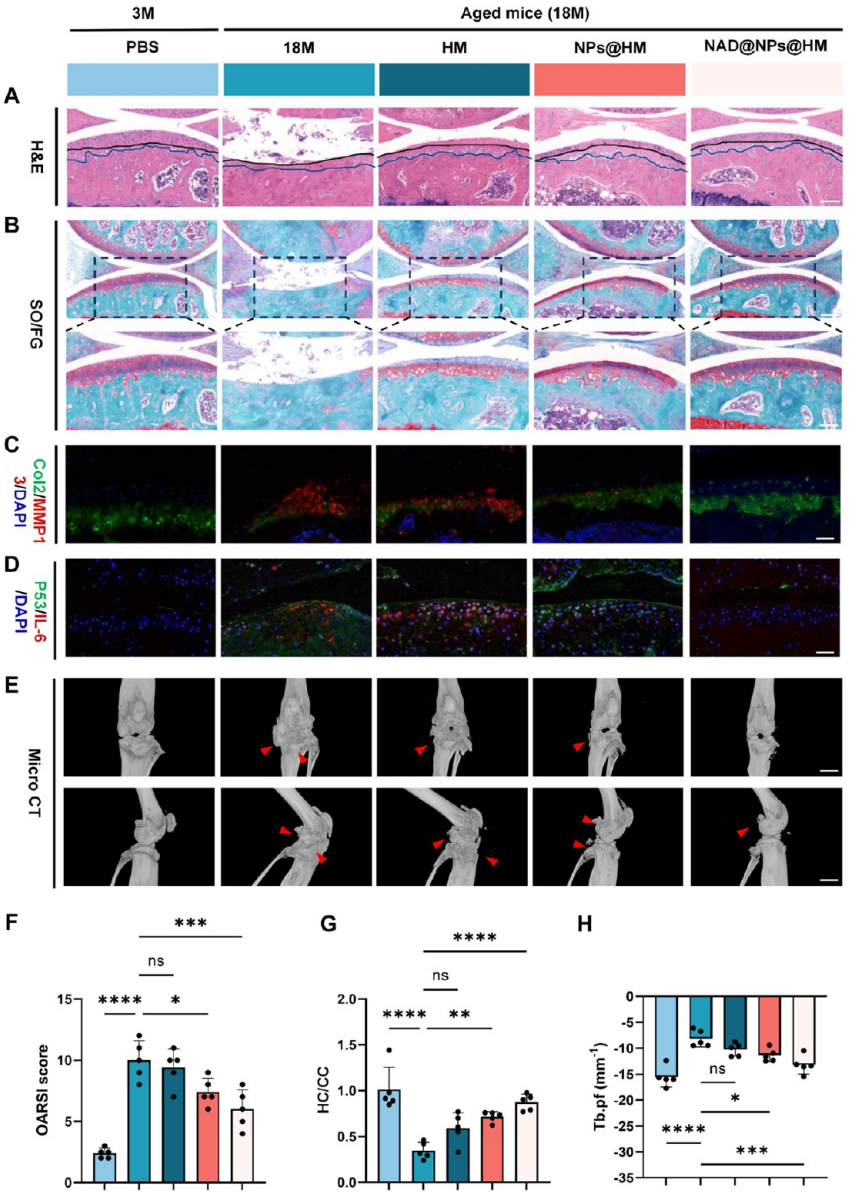

Figure 8. NAD@NPs@HM attenuates AROA progression. (A) Histomorphological micrographs illustrate H&E-stained articular cartilage sections (scale bar: 50 μm). (B) Safranin O-fast green dual staining of subchondral bone demonstrated proteoglycan deposition (red) and osseous matrix (green). Scale bar: low-magnification (100 μm); high-magnification (50 μm). (C) Multiplex immunofluorescence analysis of MMP13 (catabolic marker) and COL2A1 (anabolic marker) with DAPI nuclear counterstaining evaluated cartilage matrix homeostasis. Scale bar: 50 μm. (D) Immunostaining staining for P53, IL-6, and DAPI for assessing the senescence-associated secretory phenotype of cartilage. Scale bar: 50 μm. (E) Microcomputed tomography reconstructions illustrating medial subchondral bone microarchitecture. Scale bar: 1 mm. (F) OARSI-modified Mankin scores of articular cartilage. (G) The hyaline-calcified cartilage (HC/CC) zonal proportion within articular cartilage matrix. (H) Comparative morphometric quantification of trabecular pattern factor (Tb.pf) across subchondral bone microarchitecture was conducted in the following experimental cohorts: 3 month controls (3M), age-matched 18 month groups (18M), and therapeutic intervention arms (18 M + HM, 18 M + NPs@HM, 18 M + NAD@NPs@HM). Number of repetitions of all experiments $n \geq 3$. Data are presented as the mean ± SD (*$P < 0.05$; **$P < 0.01$; ***$P < 0.001$ and ****$P < 0.0001$).

no pathological alterations (necrosis, congestion, or hemorrhage) post-treatment (Figure S8). Comprehensive hematological profiling—encompassing erythrocyte (RBC, HGB, MCV, MCH, and MCHC) and leukocyte (WBC, Neu, Lym, and EOS) parameters, alongside platelet indices (MPV)—demonstrated all values within physiological reference ranges (Figure S9). Notably, platelet levels in elderly mice were significantly increased, consistent with previous studies,[79] whereas PLT levels returned to those of young mice after NAD@NPs@HM treatment (Figure S9). All serum biochemical markers (CREA-S, UREA, ALT, and AST) showed levels consistent with those of young controls, demonstrating no hepatorenal toxicity from hydrogel microspheres (Figure S10). Overall, all investigations demonstrated that our hydrogel microspheres exhibited favorable biocompatibility *in vivo*.

Evaluation of *In Vivo* Treatment of AROA. Intra-articular injection of hydrogel microspheres was administered to mice at 15 months of age, followed by gait analysis at 18 months to assess therapeutic efficacy, with the experimental procedures presented in Figure 7A. The gait index, encompassing gait

https://doi.org/10.1021/acsnano.5c01184
ACS Nano 2025, 19, 17606−17626

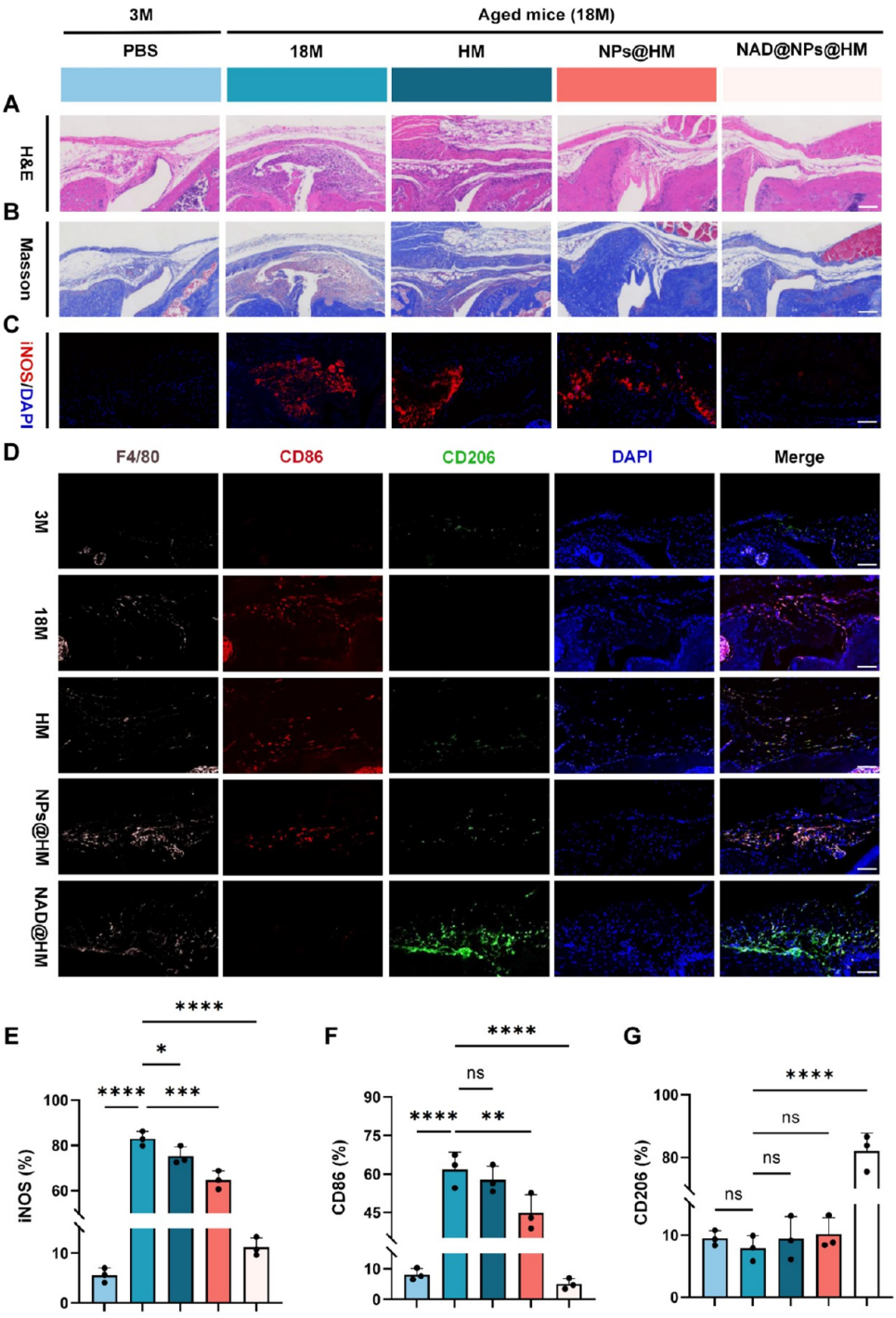

Figure 9. NAD@NPs@HM regulates the inflammatory microenvironment of knee joints in AROA. (A, B) Representative images of HE and Masson staining staining the of synovium. Scale bar: 50 μm. (C) Immunostaining for iNOS and DAPI for assessing the synovitis. Scale bar: 50 μm. (D) Immunostaining for the M1 and M2 types of synovial macrophages. Scale bar: 50 μm. (E) Quantitative analysis of iNOS expression levels in synovial membranes. (F, G) Statistical analysis for the number of $CD86^+$ macrophages and $CD206^+$ macrophages within the synovial membranes of the 3 M group, 18 M group, 18 M + HM group, 18 M + NPs@HM group, and 18 M + NAD@NPs@HM group. Quantitative data were expressed as mean ± SD (n = 3). (*P < 0.05; **P < 0.01; ***P < 0.001 and ****P < 0.0001).

screenshots and gait intensities, revealed that elderly mice exhibited higher gait intensities compared with younger samples (Figure 7B). To further investigate the changes across all treatment groups, an independent analysis was conducted specifically on the rear left limb that underwent intra-articular injection with hydrogel microspheres. This analysis yielded parameters indicative of left hind limb function, including print area, gait angle, mean stride length, mean brake time, mean stride time, and mean stance time (Figure 7C−H). Due to cartilage damage and joint pain, aged mice with OA exhibited gait abnormalities marked by a decrease in print area, an increase in gait angle, a shortening of stride length, a prolongation of stride time, an extension of brake time, and an elongation of stance time, all indicative of a reduced walking speed. In stark contrast, all therapy groups showed improvement in gait velocity, with NAD@NPs@HM exhibiting the most pro-

https://doi.org/10.1021/acsnano.5c01184
ACS Nano 2025, 19, 17606−17626

nounced therapeutic effect thanks to the effective lubrication imparted by our hydrogel microspheres. These findings suggested that intra-articular injection of hydrogel microspheres not only did not impede knee motion but also significantly improved knee joint function and gait patterns in aged mice.

To investigate the potential of NAD@NPs@HM in delaying OA progression, a range of histological staining assays were performed on cartilage tissues, including hematoxylin-eosin (H&E) staining (Figure 8A), Safranin O-fast green (SO/FG) staining (Figure 8B), and Toluidine blue staining (Figure S11A). The findings revealed that the 18 month (18M) group exhibited characteristic OA features such as surface discontinuity and erosion fissures. However, groups that received intra-articular injections of hydrogel microspheres, particularly the NAD@NPs@HM group, demonstrated notable improvements in morphological changes, matrix staining, and tidemark integrity. Specifically, the NAD@NPs@HM group showed the most favorable results, with upregulated COL2A1 levels and substantially reduced MMP13 levels (Figure 8C), as well as the most favorable OARSI score (Figure 8F), the optimal hyaluronan (HC)/collagen type II (CC) ratio (Figure 8G), and the highest relative glycosaminoglycan (GAG) content (Figure S11G) compared to other treatments. Histomorphometric analysis via Masson's trichrome staining demonstrated NAD@NPs@HM's mitigated fibrosis efficacy in a cartilaginous tissue (Figure S11B). Additionally, the SASP of the cartilage was evaluated through immunofluorescence staining of P53 and IL-6, revealing a significant decrease in these markers in the NAD@NPs@HM group compared with the 18 M and HM groups (Figure 8D). These data suggest a decrease in the number of senescent cells in the NAD@NPs@HM-treated group. Furthermore, subchondral bone degradation constitutes a central pathogenic mechanism in OA progression, driving subsequent articular cartilage deterioration.[80] We examined the impact of various treatments on the subchondral bone in elderly mice using microcomputed tomography (micro-CT) scans (Figure 8E,H). The results showed that the aging induced numerous osteophytes, which appeared (red arrows marked osteophyte) in each group of joint cavities in OA. By contrast, the NAD@NPs@HM group displayed minimal osteophytes, comparable to those in the 3 month (3M) group, but offered limited assistance in combating bone mass loss induced by AROA (Figure S11C–E).

In addition to cartilage degeneration, the study focused on the pathological changes in the synovium associated with OA. The native synovial membrane demonstrates a paucicellular histoarchitecture, featuring a discrete intimal monolayer (1–3 cell thickness) and a sparsely cellular sublining compartment. Ultrastructural analysis reveals this specialized connective tissue contains vascular channels, adipocytes, and fibroblast-like synoviocytes, with only a few macrophages.[9] Revealed by H&E and Masson staining (Figure 9A,B), synovial tissue in aged mice became proliferative and hypertrophic, with abundant cell infiltration and higher synovitis scores (Figure S11F) than normal controls. However, the synovium in the NAD@NPs@HM group showed minimal proliferation. Macrophage accumulation, as indicated by an increase in F4/80$^+$-stained cells, was observed in the synovium's intimal lining of aged mice (Figure 9D). To further investigate the effects of NAD@NPs@HM on macrophage polarization, the study conducted immunofluorescence staining to assess M1 (CD86$^+$) and M2 (CD206$^+$) phenotype markers in synovial tissues (Figure 9D). The results demonstrated that NAD@NPs@HM effectively inhibited M1 macrophage polarization and promoted M2 macrophage repolarization in the synovial tissue, as evidenced by a decrease in red fluorescence (M1) and an increase in green fluorescence (M2) in the presence of NAD@NPs@HM treatment. Additionally, NAD@NPs@HM reduced the proinflammatory mediator iNOS in synovial membranes (Figure 9C,E). Notably, while the synovitis score and the percentage of CD86$^+$ cells decreased in the NPs@HM group, there was no significant effect on the percentage of CD206$^+$ cells (Figure 9F,G). This indicated that the reprogramming of M1 into M2 macrophages was achieved through NAD regulation. In general, the above results indicate that NAD@NPs@HM exhibits a prominent performance in mitigating the progression of AROA. Therefore, this represents a desirable method for the treatment of the disease.

CONCLUSIONS

In this study, we introduce a promising and three-pronged therapeutic strategy for AROA, which involves the use of injectable hydrogel microspheres encapsulated with positively charged NAD-loaded Lf-modified nanoliposomes, designated as NAD@NPs@HM. First, these microspheres serve as biomimetic lubricants, improving gait in mice. Second, they function as reservoirs for NAD-loaded nanoliposomes, prolonging drug action time. Third, in terms of the pathogenesis of AROA, we have demonstrated through transcriptome analysis, untargeted metabolomics, and *in vivo*/*in vitro* experiments that NAD@NPs@HM can reduce cartilage aging, maintain chondrocyte metabolic balance, and alleviate synovitis by regulating the metabolic reprogramming of proinflammatory M1 macrophages into anti-inflammatory M2 macrophages. In conclusion, although further research is needed to decipher the detailed mechanisms, our study paves the way for future nonsurgical treatments of AROA.

EXPERIMENTAL SECTION

Materials. Chemical constituents, including chondroitin sulfate (ChS), lactoferrin (Lf), nicotinamide adenine dinucleotide (NAD), soy lecithin, and DSPE-mPEG2000 were acquired from Aladdin Biochemical Co., Ltd. (Shanghai, China). Cell culture components comprising Dulbecco's Modified Eagle Medium (DMEM) basal medium and fetal bovine serum (FBS) were sourced from Gibco (Thermo Fisher Scientific Inc., MA, USA). Metabolic assays including NAD$^+$/NADH quantification kit, ATP detection kit, calcein-AM/PI viability staining system, CCK-8 proliferation assay, apoptosis detection module, and senescence-associated β-galactosidase staining kit were procured from Beyotime Biotechnology (Jiangsu, China). Lipopolysaccharide (LPS) was acquired from Sigma-Aldrich (MO, USA); macrophage polarization markers (iNOS, F4/80, CD86, CD206) and extracellular matrix antibodies (COL2A1, MMP13) were acquired from Proteintech Group Inc. (Hubei, China); Alexa Fluor-conjugated secondary antibodies (488/594 nm) were acquired from Thermo Fisher Scientific (MA, USA). Histological staining systems including H&E, Masson's trichrome, Safranin O-fast Green, and Alcian blue cartilage staining kits were acquired from Solarbio Life Sciences (Beijing, China). Molecular biology reagents: RNA extraction kit was acquired from Accurate Biology (Hunan, China); EdU proliferation assay and Phalloidin-TRITC cytoskeleton probe were acquired from Yeasen Biotech (Shanghai, China); NGS library preparation kit was acquired from Hieff Biotech (Shanghai, China). Cell lines: ATDC5 chondrocytes and RAW264.7 macrophages were acquired from Merck KGaA (Darmstadt, Germany). Mounting media: Fluoroshield with DAPI was acquired from Sigma-Aldrich; neutral balsam was acquired from Sangon Biotech (Shanghai, China). All other analytical-grade chemicals were obtained from Aladdin without additional purification.

https://doi.org/10.1021/acsnano.5c01184
ACS Nano 2025, 19, 17606–17626

Preparation and Characterization of NPs. NAD@NPs were fabricated through an emulsion solvent evaporation method, where an aqueous phase containing 40 mg of NAD and 16 mg of lactoferrin in 4 mL of deionized water was emulsified with an organic phase of 4 mL of dichloromethane containing 100 mg/mL soy lecithin and 20 mg/mL DSPE-mPEG2000 under ice-cooled conditions. The emulsion was homogenized by sonication (100 W, 10 min), followed by solvent evaporation and centrifugation (8000 rpm, 15 min, 4 °C). The nanoparticles were purified through 0.1 μm polycarbonate membrane extrusion (Avanti Polar Lipids) and characterized for size distribution (DLS) and surface charge (ELS) by using a Malvern Zetasizer Nano ZS90. Morphological analysis was performed by TEM (Talos L120C) after negative staining with 1% uranyl acetate. Control nanoparticles were prepared identically without NAD incorporation. Finally, with reference to established methodologies from previous studies,[81−83] total NAD concentration was quantified using the Beyotime NAD^+/NADH Detection Kit (S0175) via the WST-8 assay, and the encapsulated drug amount was determined. Based on prior research,[47] drug encapsulation parameters were quantitatively determined using established mathematical formulations:

$$\text{encapsulation efficiency}(\%) = \frac{\text{mass of encapsulated drug}}{\text{mass of drug added}} \times 100\%$$

$$\text{drug loading capacity}(\%) = \frac{\text{mass of encapsulated drug}}{\text{mass of nanoparticles}} \times 100\%$$

Synthesis of ChSMA. ChS (2 g) was dissolved in PBS (50 mL, pH 7.4) at 25 °C, followed by dropwise addition of methacrylic anhydride (10 mL) under dark conditions at 4 °C with continuous pH maintenance (8−9) during an overnight reaction. The product was purified through 3.5 kDa MWCO dialysis against distilled water (daily replacement) for 7 days, lyophilized to obtain a white porous matrix, and characterized by ^{1}H NMR spectroscopy prior to storage at −4 °C.

Preparation and Characterization of Hydrogel Microspheres. Briefly, a 10% (w/v) ChSMA solution in PBS containing a 0.25% (w/v) LAP photoinitiator was prepared as the aqueous phase. The aqueous and oil phases were slowly infused into the microfluidic chip (DT-80, ibiochip, China) using a dual-channel syringe pump (XFP02, Zhongxinqiheng, China) at flow rates of 0.5 and 5 mL/h (inner diameter: 50 μm), respectively, achieving a droplet generation frequency of approximately 200 droplets per minute. The hydrogel microspheres were photopolymerized by 365 nm UV irradiation (6.9 mW/cm^2, 20 s), followed by sequential washing with acetone and 75% ethanol to eliminate residual oil/surfactants then PBS rinses (4 h intervals, 24 h). Microsphere morphology was characterized using optical microscopy (Olympus) and high-resolution SEM (Apreo S, Thermo Fisher), while the size distribution and surface charge were analyzed via dynamic light scattering (Malvern Nano-ZS90). Nanoliposome incorporation was achieved by blending with the ChSMA precursor solution prior to cross-linking.

Drug Release Test and Degradation Test In Vitro. Refer to previous works,[25,47] glass vials containing 5 mL of NAD@NPs@HM suspension were incubated in a 37 °C thermostatic shaker at 100 rpm, with four 3 mm diameter zirconia-grinding beads added to simulate frictional conditions. (The workflow is schematized in Figure S1H.) For the drug release study, samples were collected at predetermined time points (1, 2, 3, 7, 14, 21, and 28 days) and centrifuged (1000 × *g*, 3 min, 4 °C), and supernatants were analyzed for NAD concentration using the Beyotime NAD^+/NADH Detection Kit (S0175) via the WST-8 assay to generate release profiles. The standard curve of NAD is shown in Figure S1C. For degradation assessment, NAD@NPs@HM was suspended in PBS containing 0.2% type II collagenase (40508ES60, Yeasen) to mimic physiological enzymatic conditions. The suspension (5 mL, consistent with the drug release study) underwent identical incubation and mechanical simulation (zirconia beads, 100 rpm, 37 °C). At each time point, samples were centrifuged (1000 × *g*, 3 min, 4 °C), and the pellets were lyophilized. Residual mass was quantified using a precision electronic balance (TH7394, Kunshan Tuoheng Precision Instrument Co., Ltd., China) and compared with initial weights to evaluate degradation kinetics.

Tribological Evaluation. Friction characterization was performed on an UMT-3 tribometer (Bruker Nano, Germany) under reciprocating motion (600 cycles, ambient conditions). The pin-on-disk configuration comprised a PTFE spherical probe (5 mm bearing surface) articulating against a silicon substrate. Lubrication protocols involved dispensing 20 μL of microsphere suspensions (5 mg/mL in PBS) or PBS control at the tribocontact interface. Operational parameters included the following: 4 mm oscillatory displacement; 1 Hz reciprocating frequency; 12 N applied normal force.

Biocompatibility. Chondrocyte-macrophage cocultures (1 × 10^4 cells/well) were seeded in 24-well plates and coincubated with microspheres for 24 h. Post-treatment processing included sequential 4% paraformaldehyde fixation (15 min), 0.5% Triton X-100 permeabilization (15 min), and cytoskeletal staining with Phalloidin-TRITC in 1% BSA blocking buffer (30 min). Nuclear visualization was achieved through DAPI counterstaining (Solarbio Life Sciences, China) prior to epifluorescence microscopy (Nikon Eclipse Ti2, N31373). Parallel experiments involved calcein-AM/PI dual-staining (30 min, dark) following 24 h of material exposure for viability assessment. The live and dead cells were then visualized and imaged by using a fluorescence microscope. The captured images were then processed for quantification and statistical analysis using ImageJ software. Furthermore, in the context of the hemolysis test, healthy mouse blood was coincubated with diverse groups of materials in 1.5 mL EP tubes under thermostatic incubation at 37 °C for an hour. Following this incubation, the color changes of the solutions within each group were meticulously monitored. Subsequently, the supernatant was carefully aspirated and transferred to a fresh 96-well plate. Using a microplate reader, the OD_{540} value was measured for each well and calculate the hemolysis rate

Evaluate Chondrocyte Senescence. Cellular senescence was quantified via senescence-associated β-galactosidase (SA-β-gal) histochemistry. Chondrocytes (5 × 10^5/well) cultured in 6-well plates underwent 4% paraformaldehyde fixation (20 min), SA-β-gal substrate incubation (37 °C, 16 h), and PBS counterstaining prior to bright-field microscopy quantification. Cartilage matrix integrity was concurrently assessed through sequential histochemical protocols: 80% methanol-fixed samples received Toluidine blue staining (2 h) or underwent Safranin O-fast green staining (5 min) with acidic differentiation (0.1% HCl/ethanol, 15 s). Proteoglycan distribution and cellular morphology were documented using microscopy with semiquantitative analysis performed using ImageJ FIJI.

Imaging of Reactive Oxygen Species. RAW264.7 and ATDC5 cell lines were plated in 96-well plates (1 × 10^4 cells/well) and treated with LPS (1 μg/mL for RAW264.7; 40 μg/mL for ATDC5). After 24 h stimulation, group-specific interventions were administered followed by 30 min incubation with 10 μM DCFH-DA. Intracellular ROS generation was quantified via fluorescence microscopy using 488 nm excitation/525 nm emission parameters, with image analysis conducted in ImageJ using background-subtracted mean fluorescence intensity.

Cellular Apoptosis Assay. RAW264.7 macrophages were seeded in six-well plates (1 × 10^5 cells/well) and polarized with LPS (1 μg/mL) for 24 h. Poststimulation, group-specific interventions were administered for an additional 24 h culture. Apoptotic profiling was performed via dual Annexin V-FITC/PI staining (5 μL each in 500 μL PBS suspension), followed by flow cytometric analysis (BD FACSVerse) using 488 nm excitation with 530/575 nm emission filters. Apoptotic cells were quantified with FlowJo software (v10.8.1) applying quadrant gating strategies.

ATP Level Assay. The ATP level was evaluated by utilizing an ATP assay kit sourced from Beyotime. Prior to analysis, chondrocytes and macrophages underwent sequential processing: PBS rinsing, lysis buffer treatment, and centrifugation (12,000 × *g*, 10 min, 4 °C). Subsequently, 50 μL of the supernatant from each group was extracted and combined with 100 μL of ATP detection solution. The luminescence intensity of the mixture was then measured by using a luminescence microplate reader. ATP concentrations were normalized to total cellular protein quantified via the BCA assay.

https://doi.org/10.1021/acsnano.5c01184
ACS Nano 2025, 19, 17606−17626

NAD Level Assay. NAD level was assessed using an enhanced NAD assay kit (Beyotime, China). According to the reagent manual, the cells were washed with PBS and lysis buffer was added to the culture plate. After being centrifuged (12,000 × *g*, 10 min, 4 °C), 20 μL of supernatant from each group was extracted and mixed with 90 μL of NAD detection solution to detect absorbency at 450 nm by a microplate reader.

JC-1 Staining. Mitochondrial integrity in chondrocytes and macrophages was evaluated using a JC-1 fluorescent probe (Beyotime) through standardized membrane potential assays. Cells were loaded with JC-1 (5 μg/mL) at 37 °C for 20 min, followed by three PBS-T washes (0.1% Tween-20) to remove unbound dye. The samples were observed and imaged under an inverted fluorescence microscope manufactured by ZEISS, Germany. A decrease in the ratio of the red to green fluorescence intensity serves as an indicator of mitochondrial dysfunction.

Flow Cytometry. Intracellular immunophenotyping was performed using Fc receptor blocking buffer (5% BSA/PBS) prior to dual-color staining with FITC-conjugated anti-CD86 (Biolegend, 1:200) and APC-conjugated anti-CD206 (Biolegend, 1:200) antibodies under light-protected conditions (4 °C, 1 h). Poststaining, cells underwent three PBS washing cycles (5 min) before flow cytometric acquisition. Fluorescence data were compensated and analyzed using FlowJo v10.8.1 software.

RNA Extraction and RT-qPCR Analysis. Nucleic acid isolation commenced with AG RNAex Pro Reagent-mediated RNA extraction, followed by cDNA synthesis using the PrimeScript reverse transcription system. SYBR Green-based qPCR amplification was performed with custom-engineered primers purchased from Yeasen Biotechnology. The expression levels were normalized to the mean CT value of GAPDH. A comprehensive list of all primers utilized in the RT-qPCR is provided in Table S3.

RNA Sequencing. Transcriptome profiling commenced with Trizol-based RNA isolation, followed by nucleic acid integrity verification through RNase-free agarose gel electrophoresis and quality assessment via Agilent 2100 Bioanalyzer per manufacturer protocols. Qualified specimens underwent commercial sequencing (Gene Denovo Biotechnology) employing Illumina HiseqTM 2500/4000 platforms. Library preparation utilized Yeasen's Ultima Dual-mode mRNA Prep Kit, featuring mRNA enrichment via Oligo(dT) magnetic beads, fragmentation, and sequential cDNA synthesis: first-strand generation followed by second-strand synthesis using DNA polymerase I/RNase H system. Amplified cDNA libraries underwent PCR enrichment prior to sequencing. Differential expression analysis implemented DESeq2 (group comparisons) and edgeR (individual samples) with significance thresholds ($|FC| > 2$, $p < 0.05$). Functional enrichment of deregulated genes was interrogated through GO term analysis and Reactome pathway mapping.

Metabolome Sequencing. Macrophages from different treatment groups were collected after 24 h of cultivation under various conditions. Metabolomic profiling was initiated with cryopreservation of cellular specimens: aliquots containing 1×10^8 cells were pelleted via low-speed centrifugation (1200 × *g*, 10 min, 4 °C), flash-frozen in liquid nitrogen, and archived at −80 °C. Subsequent metabolite extraction and LC-MS analyses were contracted to Gene Denovo Biotechnology, employing an Orbitrap Exploris 120 mass spectrometer coupled to an electrospray ionization source. Raw spectral data underwent format conversion via ProteoWizard MSConvert (v3.0.6428) prior to feature extraction using the XCMS platform (v3.7.1) for peak alignment and metabolite annotation. Multivariate statistical modeling was implemented through partial least-squares-discriminant analysis (PLS-DA) using R-based computational frameworks, while structural elucidation of deregulated metabolites was performed through mass spectral library matching.

Animal Model and Treatment. This study employed male C57BL/6J mice sourced from Southern Medical University under institutional ethical approval (SMUL202406020), compliant with the guidance of the esteemed National Research Council's Guide for the Care and Use of Laboratory Animals. Aged cohorts (14 month senescence model) and young controls (3 month) were maintained in a specific pathogen-free (SPF) barrier housing with controlled photoperiod (12 h light/dark), thermoregulation (18−22 °C), and humidity (50−60%). The senescence cohort ($n = 24$) was stratified into four experimental groups ($n = 6$/group) versus young controls (3 M group, $n = 6$). Intraarticular administration protocols were implemented via a Hamilton microinjector: PBS sham injection for control groups (3 M and 18M), blank microspheres for vehicle control, NPs@HM for nanoliposome carriers, and NAD@NPs@HM for therapeutic formulations. Ad libitum access to food and water was ensured throughout the experimental timeline.

Gait Analysis. Locomotor kinematics were quantified via the DigiGait imaging platform (XL Gait Controller; Columbus Instruments, USA) following established analytical protocols.[84] In brief, each mouse was required individual subjects to traverse the test runway unimpeded, while the software captured and assessed changes in their gait. The observed indices for the rear left limb encompassed the average print area, gait angle, stride length, stride duration, braking phase, and stance phase.

Evaluation of In Vivo Retention Time. Retention time of hydrogel-encapsulated nanoliposomes was conducted through intraarticular administration of Dil-labeled formulations in murine knee joints. Fluorescence tracking using lipophilic near-infrared dye Dil (λex = 549 nm, λem = 565 nm) was performed with the IVIS Spectrum imaging platform (Xenogen, USA) at predetermined postadministration intervals.

Microcomputed Tomography Analysis. High-resolution microtomographic imaging (SkyScan 1172; Bruker) was performed on knee joint specimens at 50 kVp/200 μA with a 9 μm isotropic voxel resolution. Raw projection data underwent filtered back-projection reconstruction using NRecon v1.6, followed by morphometric analysis in CTAn v1.9 with subchondral bone compartment segmentation. Volumetric renderings were generated via μCTVol version 2.0 using 3D adaptive histogram equalization. Quantitative trabecular architecture parameters (Tb.Pf, BV/TV, SBP.Th) were derived from the entire calcified zone spanning the osteochondral junction to a 500 μm subchondral depth.

Histological Evaluation. Specimens underwent 24 h fixation in 4% paraformaldehyde (PFA, pH 7.4) followed by EDTA-based decalcification (10% w/v, pH 7.4) under constant agitation (80 rpm, 37 °C) for 7 days. Paraffin embedding was performed after ethanol gradient dehydration. Coronal sections (5 μm) were subjected to multiplex histological staining (H&E, Masson's trichrome, Safranin O/fast green, Toluidine blue) for cartilage architecture evaluation. Calcified/hyaline cartilage (CC/HC) thickness ratios were quantified via OARSI-modified Mankin criteria. Systemic biocompatibility was assessed through H&E-stained visceral organ sections (heart, liver, spleen, lung, kidney) combined with hematological/biochemical profiling (complete blood count, ALT, AST, BUN, creatinine) across experimental cohorts.

Immunofluorescence Staining. Following deparaffinization and graded ethanol rehydration, antigen retrieval was performed using Tris-EDTA buffer (pH 9.0) at 75 °C for 45 min. Nonspecific binding was blocked with 5% BSA (Beyotime) prior to overnight incubation (4 °C) with primary antisera (1:500 dilution in blocking buffer) targeting collagen II, MMP13, P53, IL-6, iNOS, CD86, CD206, and F4/80. Fluorophore-conjugated secondary antibodies (Proteintech; Alexa Fluor 488/594/700, 1:1000) were applied for 2 h at room temperature. Multiplex immunofluorescence was achieved through tyramide-based signal amplification (AFIHC026, Hunan Aifang Biological Technology, China) with subsequent nuclear counterstaining using a Hoechst 33342 instrument (Solarbio). The tissue and cell sample slides were photographed using a fluorescence microscope (Nikon N31373) followed by quantitative analysis of mean fluorescence intensity (MFI) using an ImageJ FIJI distribution.

Statistical Analysis. All statistical analyses and data visualizations were performed using GraphPad Prism version 9.0 (GraphPad Software, La Jolla, CA). Data are shown as mean ± standard deviation (SD). Multiple comparisons for more than two groups were analyzed using multiple−factorial analysis of variance (ANOVA) to determine the statistically significant differences. Student's *t* test or Welch's *t* test was employed to determine the statistically significant differences between the two groups up to the homogeneity of variance. $^*P < 0.05$;

https://doi.org/10.1021/acsnano.5c01184
ACS Nano 2025, 19, 17606−17626

**$P < 0.01$; ***$P < 0.001$ and ****$P < 0.0001$ were considered to be significant.

ASSOCIATED CONTENT

Supporting Information

The Supporting Information is available free of charge at https://pubs.acs.org/doi/10.1021/acsnano.5c01184.

Characterization of the nanoliposomes and the hydrogel microspheres, the primer sequences used to RT-qPCR, the results of molecular docking, standard curve, IVIS images, JC-1 and mtROS staining, transcriptomics and metabolomics of macrophages, cross talk of macrophages and chondrocytes, HE staining of major organs, blood routine and biochemistry analysis, Toluidine blue staining and Masson staining, and quantitative analysis of micro-CT (PDF)

AUTHOR INFORMATION

Corresponding Authors

Daogang Guan − *Department of Biochemistry and Molecular Biology, School of Basic Medical Sciences and Guangdong Provincial Key Laboratory of Single Cell Technology and Application, Southern Medical University, Guangzhou 510515, P. R. China*; Email: guandg0929@smu.edu.cn

Genggeng Qin − *Department of Radiology, Nanfang Hospital, Southern Medical University, Guangzhou, Guangdong 510515, P. R. China*; Email: zealotq@smu.edu.cn

Weiguo Chen − *Department of Radiology, Nanfang Hospital, Southern Medical University, Guangzhou, Guangdong 510515, P. R. China*; orcid.org/0000-0003-1552-0511; Email: chen1999@smu.edu.cn

Authors

Yanpeng Lin − *Department of Radiology, Nanfang Hospital, Southern Medical University, Guangzhou, Guangdong 510515, P. R. China*

Hangtian Wu − *Division of Orthopaedics and Traumatology, Department of Orthopaedics, Nanfang Hospital, Southern Medical University, Guangzhou, Guangdong 510515, P. R. China*

Jun Wang − *School of Animal Science and Technology, Foshan University, Foshan, Guangdong 528231, People's Republic of China*

Wanling He − *Department of Biochemistry and Molecular Biology, School of Basic Medical Sciences and Guangdong Provincial Key Laboratory of Single Cell Technology and Application, Southern Medical University, Guangzhou 510515, P. R. China*

Jiahui Hou − *Division of Orthopaedics and Traumatology, Department of Orthopaedics, Nanfang Hospital, Southern Medical University, Guangzhou, Guangdong 510515, P. R. China*

Vidmi Taolam Martin − *Division of Orthopaedics and Traumatology, Department of Orthopaedics, Nanfang Hospital, Southern Medical University, Guangzhou, Guangdong 510515, P. R. China*

Chencheng Zhu − *Division of Orthopaedics and Traumatology, Department of Orthopaedics, Nanfang Hospital, Southern Medical University, Guangzhou, Guangdong 510515, P. R. China*

Yupeng Chen − *Department of Biochemistry and Molecular Biology, School of Basic Medical Sciences and Guangdong Provincial Key Laboratory of Single Cell Technology and Application, Southern Medical University, Guangzhou 510515, P. R. China*

Junyuan Zhong − *Department of Medical Imaging, Ganzhou People's Hospital, Ganzhou, Jiangxi 341000, P. R. China*

Bin Yu − *Division of Orthopaedics and Traumatology, Department of Orthopaedics, Nanfang Hospital, Southern Medical University, Guangzhou, Guangdong 510515, P. R. China*

Aiping Lu − *Institute of Integrated Bioinformedicine and Translational Science, Hong Kong Baptist University, Hong Kong 999077, P. R. China; Guangdong-Hong Kong-Macau Joint Lab on Chinese Medicine and Immune Disease Research, Guangzhou 510515, P. R. China*

Complete contact information is available at: https://pubs.acs.org/10.1021/acsnano.5c01184

Author Contributions

▲Y.L., H.W., and J.W. contributed equally to this work. The graphics presented in this article were designed and created by H.W. using the BioRender online platform (https://BioRender.com/rr8tovk). The entire creation process and usage authorization strictly comply with BioRender's Terms of Service and Academic License Agreement. B.Y, A.L., D.G., G.Q., and W.C. conceived and designed the experiments. H.W., J.W., V.T.M., and Y.L. performed and wrote the manuscript. H.W., Y.L., J.W., W.H., and Y.C. analyzed the data. W.H., J.H., and C.Z. prepared all the figures. All authors reviewed and agreed upon the manuscript.

Notes

The authors declare no competing financial interest.

ACKNOWLEDGMENTS

This study was supported by the Science and Technology Project of Ganzhou, China (2022-ZD1373, and 2022-RC1349), the Provincial Natural Science Foundation of Guangdong, China (2022A1515110904, 2022A1515110221, 2024A1515011520, and 2024A1515011417), National Key Research and Development Program of China (2022YFC2504305), and the National Natural Science Foundation of China (82171929).

REFERENCES

(1) Johnson, V. L.; Hunter, D. J. The epidemiology of osteoarthritis. *Best Pract. Res. Clin. Rheumatol.* **2014**, *28* (1), 5−15.

(2) Loeser, R. F.; Goldring, S. R.; Scanzello, C. R.; Goldring, M. B. Osteoarthritis: a disease of the joint as an organ. *Arthritis Rheum* **2012**, *64* (6), 1697−1707.

(3) Carr, A. J.; Robertsson, O.; Graves, S.; Price, A. J.; Arden, N. K.; Judge, A.; Beard, D. J. Knee replacement. *Lancet* **2012**, *379* (9823), 1331−1340.

(4) Bijlsma, J. W.; Berenbaum, F.; Lafeber, F. P. Osteoarthritis: an update with relevance for clinical practice. *Lancet* **2011**, *377* (9783), 2115−2126.

(5) He, S.; Sharpless, N. E. Senescence in health and disease. *Cell* **2017**, *169* (6), 1000−1011.

(6) López-Otín, C.; Blasco, M. A.; Partridge, L.; Serrano, M.; Kroemer, G. Hallmarks of aging: an expanding universe. *Cell* **2023**, *186* (2), 243−278.

(7) Xie, J.; Wang, Y.; Lu, L.; Liu, L.; Yu, X.; Pei, F. Cellular senescence in knee osteoarthritis: molecular mechanisms and therapeutic implications. *Ageing Res. Rev.* **2021**, *70*, No. 101413.

(8) Charalambous, C. Articular cartilage. Part ii: degeneration and osteoarthrosis, repair, regeneration, and transplantation. In *Classic*

Papers in Orthopaedics; Banaszkiewicz, P. A.; Kader, D. F., Eds.; Springer London: London, 2014; pp 389−391. DOI: .
(9) Smith, M. D.; Barg, E.; Weedon, H.; Papengelis, V.; Smeets, T.; Tak, P. P.; Kraan, M.; Coleman, M.; Ahern, M. J. Microarchitecture and protective mechanisms in synovial tissue from clinically and arthroscopically normal knee joints. *Ann. Rheum. Dis.* **2003**, *62* (4), 303−307.
(10) Sellam, J.; Berenbaum, F. The role of synovitis in pathophysiology and clinical symptoms of osteoarthritis. *Nat. Rev. Rheumatol.* **2010**, *6* (11), 625−635.
(11) Seror, J.; Zhu, L.; Goldberg, R.; Day, A. J.; Klein, J. Supramolecular synergy in the boundary lubrication of synovial joints. *Nat. Commun.* **2015**, *6*, 6497.
(12) Dahl, L. B.; Dahl, I. M.; Engstrom-Laurent, A.; Granath, K. Concentration and molecular weight of sodium hyaluronate in synovial fluid from patients with rheumatoid arthritis and other arthropathies. *Ann. Rheum. Dis.* **1985**, *44* (12), 817−822.
(13) Fragassi, A.; Greco, A.; Palomba, R. Lubricant strategies in osteoarthritis treatment: transitioning from natural lubricants to drug delivery particles with lubricant properties. *J. Xenobiotics* **2024**, *14* (3), 1268−1292.
(14) Yan, Y.; Sun, T.; Zhang, H.; Ji, X.; Sun, Y.; Zhao, X.; Deng, L.; Qi, J.; Cui, W.; Santos, H. A.; et al. Euryale ferox seed-inspired superlubricated nanoparticles for treatment of osteoarthritis. *Adv. Funct. Mater.* **2019**, *29* (4), 1807559.
(15) Belenky, P.; Bogan, K. L.; Brenner, C. Nad+ metabolism in health and disease. *Trends Biochem. Sci.* **2007**, *32* (1), 12−19.
(16) Bonkowski, M. S.; Sinclair, D. A. Slowing ageing by design: the rise of nad(+) and sirtuin-activating compounds. *Nat. Rev. Mol. Cell Biol.* **2016**, *17* (11), 679−690.
(17) Ratajczak, J.; Joffraud, M.; Trammell, S. A.; Ras, R.; Canela, N.; Boutant, M.; Kulkarni, S. S.; Rodrigues, M.; Redpath, P.; Migaud, M. E.; et al. Nrk1 controls nicotinamide mononucleotide and nicotinamide riboside metabolism in mammalian cells. *Nat. Commun.* **2016**, *7*, 13103.
(18) Ma, Y.; Zhang, Y.; Liu, X.; Yang, X.; Guo, H.; Ding, X.; Ye, C.; Guo, C. Deletion of cd38 mitigates the severity of nec in experimental settings by modulating macrophage-mediated inflammation. *Redox Biol.* **2024**, *77*, No. 103336.
(19) Rissiek, B.; Guse, A. H.; Adriouch, S.; Bruzzone, S. Editorial: the versatile role of nicotinamide adenine dinucleotide in immunity. *Front. Immunol.* **2021**, *12*, No. 810280.
(20) Gil Alabarse, A.; Chen, L. Y.; Oliveira, P.; Qin, H.; Liu-Bryan, R. Targeting cd38 to suppress osteoarthritis development and associated pain after joint injury in mice. *Arthritis Rheumatol.* **2023**, *75* (3), 364−374.
(21) Imai, S.; Guarente, L. Nad+ and sirtuins in aging and disease. *Trends Cell Biol.* **2014**, *24* (8), 464−471.
(22) Ye, M.; Zhao, Y.; Wang, Y.; Xie, R.; Tong, Y.; Sauer, J. D.; Gong, S. Nad(h)-loaded nanoparticles for efficient sepsis therapy via modulating immune and vascular homeostasis. *Nat. Nanotechnol.* **2022**, *17* (8), 880−890.
(23) Jones, I. A.; Togashi, R.; Wilson, M. L.; Heckmann, N.; Vangsness, C. J. Intra-articular treatment options for knee osteoarthritis. *Nat. Rev. Rheumatol.* **2019**, *15* (2), 77−90.
(24) Elzoghby, A. O.; Abdelmoneem, M. A.; Hassanin, I. A.; Abd Elwakil, M. M.; Elnaggar, M. A.; Mokhtar, S.; Fang, J. Y.; Elkhodairy, K. A. Lactoferrin, a multi-functional glycoprotein: active therapeutic, drug nanocarrier & targeting ligand. *Biomaterials* **2020**, *263*, No. 120355.
(25) Hou, J.; Lin, Y.; Zhu, C.; Chen, Y.; Lin, R.; Lin, H.; Liu, D.; Guan, D.; Yu, B.; Wang, J.; et al. Zwitterion-lubricated hydrogel microspheres encapsulated with metformin ameliorate age-associated osteoarthritis. *Adv. Sci.* **2024**, *11* (30), No. e2402477.
(26) Yang, J.; Han, Y.; Lin, J.; Zhu, Y.; Wang, F.; Deng, L.; Zhang, H.; Xu, X.; Cui, W. Ball-bearing-inspired polyampholyte-modified microspheres as bio-lubricants attenuate osteoarthritis. *Small* **2020**, *16* (44), No. e2004519.
(27) Large, D. E.; Abdelmessih, R. G.; Fink, E. A.; Auguste, D. T. Liposome composition in drug delivery design, synthesis, characterization, and clinical application. *Adv. Drug Delivery Rev.* **2021**, *176*, No. 113851.
(28) He, X.; He, S.; Xiang, G.; Deng, L.; Zhang, H.; Wang, Y.; Li, J.; Lu, H. Precise lubrication and protection of cartilage damage by targeting hydrogel microsphere. *Adv. Mater.* **2024**, *36* (40), No. e2405943.
(29) Zhu, L.; Seror, J.; Day, A. J.; Kampf, N.; Klein, J. Ultra-low friction between boundary layers of hyaluronan-phosphatidylcholine complexes. *Acta Biomater.* **2017**, *59*, 283−292.
(30) Goldberg, R.; Schroeder, A.; Barenholz, Y.; Klein, J. Interactions between adsorbed hydrogenated soy phosphatidylcholine (hspc) vesicles at physiologically high pressures and salt concentrations. *Biophys. J.* **2011**, *100* (10), 2403−2411.
(31) Lei, Y.; Wang, X.; Liao, J.; Shen, J.; Li, Y.; Cai, Z.; Hu, N.; Luo, X.; Cui, W.; Huang, W. Shear-responsive boundary-lubricated hydrogels attenuate osteoarthritis. *Bioact. Mater.* **2022**, *16*, 472−484.
(32) Liu, L.; Xian, Y.; Wang, W.; Huang, L.; Fan, J.; Ma, W.; Li, Y.; Liu, H.; Yu, J. K.; Wu, D. Meniscus-inspired self-lubricating and friction-responsive hydrogels for protecting articular cartilage and improving exercise. *ACS Nano* **2023**, *17* (23), 24308−24319.
(33) Stefani, R. M.; Lee, A. J.; Tan, A. R.; Halder, S. S.; Hu, Y.; Guo, X. E.; Stoker, A. M.; Ateshian, G. A.; Marra, K. G.; Cook, J. L.; et al. Sustained low-dose dexamethasone delivery via a plga microsphere-embedded agarose implant for enhanced osteochondral repair. *Acta Biomater.* **2020**, *102*, 326−340.
(34) Vedadghavami, A.; Wagner, E. K.; Mehta, S.; He, T.; Zhang, C.; Bajpayee, A. G. Cartilage penetrating cationic peptide carriers for applications in drug delivery to avascular negatively charged tissues. *Acta Biomater.* **2019**, *93*, 258−269.
(35) Sterner, B.; Harms, M.; Woll, S.; Weigandt, M.; Windbergs, M.; Lehr, C. M. The effect of polymer size and charge of molecules on permeation through synovial membrane and accumulation in hyaline articular cartilage. *Eur. J. Pharm. Biopharm.* **2016**, *101*, 126−136.
(36) Lin, W.; Kluzek, M.; Iuster, N.; Shimoni, E.; Kampf, N.; Goldberg, R.; Klein, J. Cartilage-inspired, lipid-based boundary-lubricated hydrogels. *Science* **2020**, *370* (6514), 335−338.
(37) Corradetti, B.; Taraballi, F.; Minardi, S.; Van Eps, J.; Cabrera, F.; Francis, L. W.; Gazze, S. A.; Ferrari, M.; Weiner, B. K.; Tasciotti, E. Chondroitin sulfate immobilized on a biomimetic scaffold modulates inflammation while driving chondrogenesis. *Stem Cells Transl. Med.* **2016**, *5* (5), 670−682.
(38) Lee, J. Y.; Lee, S. H.; Kim, H. J.; Ha, J. M.; Lee, S. H.; Lee, J. H.; Ha, B. J. The preventive inhibition of chondroitin sulfate against the ccl4-induced oxidative stress of subcellular level. *Arch. Pharm. Res.* **2004**, *27* (3), 340−345.
(39) Temple-Wong, M. M.; Ren, S.; Quach, P.; Hansen, B. C.; Chen, A. C.; Hasegawa, A.; D'Lima, D. D.; Koziol, J.; Masuda, K.; Lotz, M. K.; et al. Hyaluronan concentration and size distribution in human knee synovial fluid: variations with age and cartilage degeneration. *Arthritis Res. Ther.* **2016**, *18*, 18.
(40) Mueller, P. A.; Zhu, L.; Tavori, H.; Huynh, K.; Giunzioni, I.; Stafford, J. M.; Linton, M. F.; Fazio, S. Deletion of macrophage low-density lipoprotein receptor-related protein 1 (lrp1) accelerates atherosclerosis regression and increases c-c chemokine receptor type 7 (ccr7) expression in plaque macrophages. *Circulation* **2018**, *138* (17), 1850−1863.
(41) Zhao, Y.; Yang, Y.; Zhang, J.; Wang, R.; Cheng, B.; Kalambhe, D.; Wang, Y.; Gu, Z.; Chen, D.; Wang, B.; et al. Lactoferrin-mediated macrophage targeting delivery and patchouli alcohol-based therapeutic strategy for inflammatory bowel diseases. *Acta Pharm. Sin. B* **2020**, *10* (10), 1966−1976.
(42) Vedadghavami, A.; He, T.; Zhang, C.; Amiji, S. M.; Hakim, B.; Bajpayee, A. G. Charge-based drug delivery to cartilage: hydrophobic and not electrostatic interactions are the dominant cause of competitive binding of cationic carriers in synovial fluid. *Acta Biomater.* **2022**, *151*, 278−289.
(43) Lin, J.; Hu, W.; Gao, T.; Bao, B.; Li, X.; Huang, T.; Sun, Y.; Shen, J.; Xu, H.; Zhu, K.; et al. E-poly-l-lysine as an efficient cartilage

https://doi.org/10.1021/acsnano.5c01184
ACS Nano 2025, 19, 17606−17626

penetrating and residing drug carrier with high intraarticular injection safety for treating osteoarthritis. *Chem. Eng. J.* **2022**, *430*, No. 133018.
(44) Ewert, K. K.; Scodeller, P.; Simon-Gracia, L.; Steffes, V. M.; Wonder, E. A.; Teesalu, T.; Safinya, C. R. Cationic liposomes as vectors for nucleic acid and hydrophobic drug therapeutics. *Pharmaceutics* **2021**, *13* (9), 1365.
(45) Evans, C. H.; Kraus, V. B.; Setton, L. A. Progress in intra-articular therapy. *Nat. Rev. Rheumatol.* **2014**, *10* (1), 11−22.
(46) Karaz, S.; Akay, G.; Karaoglu, I. C.; Han, M.; Nizamoglu, S.; Kizilel, S.; Senses, E. Shear-triggered release of lipid nanoparticles from tissue-mimetic hydrogels. *Macromol. Rapid Commun.* **2023**, *44* (13), No. e2300090.
(47) He, Y.; Sun, M.; Wang, J.; Yang, X.; Lin, C.; Ge, L.; Ying, C.; Xu, K.; Liu, A.; Wu, L. Chondroitin sulfate microspheres anchored with drug-loaded liposomes play a dual antioxidant role in the treatment of osteoarthritis. *Acta Biomater.* **2022**, *151*, 512−527.
(48) Li, X.; Dai, B.; Guo, J.; Zheng, L.; Guo, Q.; Peng, J.; Xu, J.; Qin, L. Nanoparticle-cartilage interaction: pathology-based intra-articular drug delivery for osteoarthritis therapy. *Nano-Micro Lett.* **2021**, *13* (1), 149.
(49) Diekman, B. O.; Sessions, G. A.; Collins, J. A.; Knecht, A. K.; Strum, S. L.; Mitin, N. K.; Carlson, C. S.; Loeser, R. F.; Sharpless, N. E. Expression of p16(ink)(4a) is a biomarker of chondrocyte aging but does not cause osteoarthritis. *Aging Cell* **2018**, *17* (4), No. e12771.
(50) Hayflick, L.; Moorhead, P. S. The serial cultivation of human diploid cell strains. *Exp. Cell Res.* **1961**, *25* (3), 585−621.
(51) D'Amico, D.; Olmer, M.; Fouassier, A. M.; Valdes, P.; Andreux, P. A.; Rinsch, C.; Lotz, M. Urolithin a improves mitochondrial health, reduces cartilage degeneration, and alleviates pain in osteoarthritis. *Aging Cell* **2022**, *21* (8), No. e13662.
(52) An, D.; Zeng, Q.; Zhang, P.; Ma, Z.; Zhang, H.; Liu, Z.; Li, J.; Ren, H.; Xu, D. Alpha-ketoglutarate ameliorates pressure overload-induced chronic cardiac dysfunction in mice. *Redox Biol.* **2021**, *46*, No. 102088.
(53) Blanco, F. J.; Rego, I.; Ruiz-Romero, C. The role of mitochondria in osteoarthritis. *Nat. Rev. Rheumatol.* **2011**, *7* (3), 161−169.
(54) Gorgoulis, V.; Adams, P. D.; Alimonti, A.; Bennett, D. C.; Bischof, O.; Bishop, C.; Campisi, J.; Collado, M.; Evangelou, K.; Ferbeyre, G.; et al. Cellular senescence: defining a path forward. *Cell* **2019**, *179* (4), 813−827.
(55) Blanco, F. J.; Valdes, A. M.; Rego-Perez, I. Mitochondrial dna variation and the pathogenesis of osteoarthritis phenotypes. *Nat. Rev. Rheumatol.* **2018**, *14* (6), 327−340.
(56) Berry, B. J.; Vodickova, A.; Muller-Eigner, A.; Meng, C.; Ludwig, C.; Kaeberlein, M.; Peleg, S.; Wojtovich, A. P. Optogenetic rejuvenation of mitochondrial membrane potential extends c. *Elegans lifespan. Nat. Aging* **2023**, *3* (2), 157−161.
(57) Coryell, P. R.; Diekman, B. O.; Loeser, R. F. Mechanisms and therapeutic implications of cellular senescence in osteoarthritis. *Nat. Rev. Rheumatol.* **2021**, *17* (1), 47−57.
(58) Robinson, W. H.; Lepus, C. M.; Wang, Q.; Raghu, H.; Mao, R.; Lindstrom, T. M.; Sokolove, J. Low-grade inflammation as a key mediator of the pathogenesis of osteoarthritis. *Nat. Rev. Rheumatol.* **2016**, *12* (10), 580−592.
(59) Gaigeard, N.; Cardon, A.; Le Goff, B.; Guicheux, J.; Boutet, M. Unveiling the macrophage dynamics in osteoarthritic joints: from inflammation to therapeutic strategies. *Drug Discovery Today* **2024**, *29* (11), No. 104187.
(60) Hsueh, M. F.; Zhang, X.; Wellman, S. S.; Bolognesi, M. P.; Kraus, V. B. Synergistic roles of macrophages and neutrophils in osteoarthritis progression. *Arthritis Rheumatol.* **2021**, *73* (1), 89−99.
(61) Van Gool, F.; Galli, M.; Gueydan, C.; Kruys, V.; Prevot, P. P.; Bedalov, A.; Mostoslavsky, R.; Alt, F. W.; De Smedt, T.; Leo, O. Intracellular nad levels regulate tumor necrosis factor protein synthesis in a sirtuin-dependent manner. *Nat. Med.* **2009**, *15* (2), 206−210.
(62) Gerner, R. R.; Klepsch, V.; Macheiner, S.; Arnhard, K.; Adolph, T. E.; Grander, C.; Wieser, V.; Pfister, A.; Moser, P.; Hermann-Kleiter, N.; et al. Nad metabolism fuels human and mouse intestinal inflammation. *Gut* **2018**, *67* (10), 1813−1823.
(63) Daghestani, H. N.; Pieper, C. F.; Kraus, V. B. Soluble macrophage biomarkers indicate inflammatory phenotypes in patients with knee osteoarthritis. *Arthritis Rheumatol.* **2015**, *67* (4), 956−965.
(64) Lucas, K.; Maes, M. Role of the toll like receptor (tlr) radical cycle in chronic inflammation: possible treatments targeting the tlr4 pathway. *Mol. Neurobiol.* **2013**, *48* (1), 190−204.
(65) Yuan, Y.; Chen, Y.; Peng, T.; Li, L.; Zhu, W.; Liu, F.; Liu, S.; An, X.; Luo, R.; Cheng, J.; et al. Mitochondrial ros-induced lysosomal dysfunction impairs autophagic flux and contributes to m1 macrophage polarization in a diabetic condition. *Clin. Sci. (Lond).* **2019**, *133* (15), 1759−1777.
(66) Kraus, V. B.; Mcdaniel, G.; Huebner, J. L.; Stabler, T. V.; Pieper, C. F.; Shipes, S. W.; Petry, N. A.; Low, P. S.; Shen, J.; Mcnearney, T. A.; et al. Direct in vivo evidence of activated macrophages in human osteoarthritis. *Osteoarthritis Cartilage* **2016**, *24* (9), 1613−1621.
(67) Sanchez-Lopez, E.; Coras, R.; Torres, A.; Lane, N. E.; Guma, M. Synovial inflammation in osteoarthritis progression. *Nat. Rev. Rheumatol.* **2022**, *18* (5), 258−275.
(68) Bi, J.; Zhang, C.; Lu, C.; Mo, C.; Zeng, J.; Yao, M.; Jia, B.; Liu, Z.; Yuan, P.; Xu, S. Age-related bone diseases: role of inflammaging. *J. Autoimmun.* **2024**, *143*, No. 103169.
(69) Henry, B. D.; Neill, D. R.; Becker, K. A.; Gore, S.; Bricio-Moreno, L.; Ziobro, R.; Edwards, M. J.; Muhlemann, K.; Steinmann, J.; Kleuser, B.; et al. Engineered liposomes sequester bacterial exotoxins and protect from severe invasive infections in mice. *Nat. Biotechnol.* **2015**, *33* (1), 81−88.
(70) Ou, A.; Zhang, J.; Fang, Y.; Wang, R.; Tang, X.; Zhao, P.; Zhao, Y.; Zhang, M.; Huang, Y. Disulfiram-loaded lactoferrin nanoparticles for treating inflammatory diseases. *Acta Pharmacol. Sin.* **2021**, *42* (11), 1913−1920.
(71) Roskoski, R. J. Src protein-tyrosine kinase structure, mechanism, and small molecule inhibitors. *Pharmacol. Res.* **2015**, *94*, 9−25.
(72) Chen, Z.; Xiao, Y.; Yang, P.; Wang, R. Pan-cancer analysis reveals src may link lipid metabolism and macrophages. *Iran. J. Biotechnol.* **2023**, *21* (2), No. e3325.
(73) Yang, W. S.; Lee, J.; Kim, T. W.; Kim, J. H.; Lee, S.; Rhee, M. H.; Hong, S.; Cho, J. Y. Src/nf-kappab-targeted inhibition of lps-induced macrophage activation and dextran sodium sulphate-induced colitis by archidendron clypearia methanol extract. *J. Ethnopharmacol.* **2012**, *142* (1), 287−293.
(74) Wu, J.; Wang, Y.; Yang, Y.; Liu, F.; Jiang, Z.; Jiang, Z. Tnfsf9 promotes metastasis of pancreatic cancer by regulating m2 polarization of macrophages through src/fak/p-akt/il-1β signaling. *Int. Immunopharmacol.* **2022**, *102*, No. 108429.
(75) Rodriguez-Prados, J. C.; Traves, P. G.; Cuenca, J.; Rico, D.; Aragones, J.; Martin-Sanz, P.; Cascante, M.; Bosca, L. Substrate fate in activated macrophages: a comparison between innate, classic, and alternative activation. *J. Immunol.* **2010**, *185* (1), 605−614.
(76) Odegaard, J. I.; Chawla, A. Alternative macrophage activation and metabolism. *Annu. Rev. Pathol.* **2011**, *6*, 275−297.
(77) Huang, S. C.; Everts, B.; Ivanova, Y.; O'Sullivan, D.; Nascimento, M.; Smith, A. M.; Beatty, W.; Love-Gregory, L.; Lam, W. Y.; O'Neill, C. M.; et al. Cell-intrinsic lysosomal lipolysis is essential for alternative activation of macrophages. *Nat. Immunol.* **2014**, *15* (9), 846−855.
(78) Zhang, J.; Wang, S.; Jiang, B.; Huang, L.; Ji, Z.; Li, X.; Zhou, H.; Han, A.; Chen, A.; Wu, Y.; et al. C-src phosphorylation and activation of hexokinase promotes tumorigenesis and metastasis. *Nat. Commun.* **2017**, *8*, 13732.
(79) Dayal, S.; Wilson, K. M.; Motto, D. G.; Miller, F. J.; Chauhan, A. K.; Lentz, S. R. Hydrogen peroxide promotes aging-related platelet hyperactivation and thrombosis. *Circulation* **2013**, *127* (12), 1308−1316.
(80) Cui, Z.; Wu, H.; Xiao, Y.; Xu, T.; Jia, J.; Lin, H.; Lin, R.; Chen, K.; Lin, Y.; Li, K.; et al. Endothelial pdgf-bb/pdgfr-beta signaling promotes osteoarthritis by enhancing angiogenesis-dependent abnormal subchondral bone formation. *Bone Res.* **2022**, *10* (1), 58.
(81) Li, C.; Wu, B.; Li, Y.; Chen, J.; Ye, Z.; Tian, X.; Wang, J.; Xu, X.; Pan, S.; Zheng, Y.; et al. Amino acid catabolism regulates hematopoietic

stem cell proteostasis via a gcn2-eif2alpha axis. *Cell Stem Cell* **2022**, *29* (7), 1119−1134.
(82) Xia, J.; Zhang, J.; Wu, X.; Du, W.; Zhu, Y.; Liu, X.; Liu, Z.; Meng, B.; Guo, J.; Yang, Q.; et al. Blocking glycine utilization inhibits multiple myeloma progression by disrupting glutathione balance. *Nat. Commun.* **2022**, *13* (1), 4007.
(83) Li, M.; Lai, Y.; Chen, B.; Guo, C.; Zhou, M.; Zhao, S.; Wang, S.; Li, J.; Yang, N.; Zhang, H. Nampt is a metabolic checkpoint of ifngamma-producing cd4(+) t cells in lupus nephritis. *Mol. Ther.* **2023**, *31* (1), 193−210.
(84) Xue, C.; Tian, J.; Cui, Z.; Liu, Y.; Sun, D.; Xiong, M.; Yi, N.; Wang, K.; Li, X.; Wang, Y.; et al. Reactive oxygen species (ros)-mediated m1 macrophage-dependent nanomedicine remodels inflammatory microenvironment for osteoarthritis recession. *Bioact. Mater.* **2024**, *33*, 545−561.

https://doi.org/10.1021/acsnano.5c01184
ACS Nano 2025, 19, 17606−17626